Chapter 2: State, variability and change in the marine environment: new monitoring indicators

2.1. Sea surface winds and Ekman pumping

Authors: Maria Belmonte Rivas, Ad Stoffelen, Abderrahim Bentamy

Statement of main outcome: Sea surface wind stress and Ekman transport changes are assessed that imply changes in both large-scale and smaller-scale ocean forcing. During 2017 a transition from gradually warming El Niño Southern Oscillation conditions to non-El-Niño-Southern-Oscillation conditions in the tropical Pacific is observed. The North Atlantic is influenced by sustained high North Atlantic Oscillation conditions, with higher-than-average Azores High and south-easterly wind anomalies in the Labrador Sea. We note sustained high westerlies in the Southern Ocean, and increased south-easterly trades in the South Indian Ocean, with enhanced wind convergence off Sumatra. Trends and anomalies in Ekman pumping (ocean circulation forcing) are consistent with the respective trends and anomalies observed in the wind. Inter-annual variability is dominated by changes in mean large-scale conditions, rather than changes in transient smaller-scale wind activity, without any substantial trends in globally averaged annual mean or transient winds. Regional trends and anomalies in wind variability are generally of opposite sign to those in the mean wind, as they feed on the mean flow and counterbalance it. These wind stress changes imply changes in both large-scale and smaller-scale ocean forcing.

Products used

Ref. No.	Product name and type	Documentation
2.1.1	Product: WIND_GLO_WIND_L3_REP_OBSERVATIONS_012_005/ Dataset (reprocessed ASCAT-A 25 km Ascending): KNMI-GLO-WIND_L3-REP-OBS_METOP-A_ASCAT_25_ASC Remote sensing	PUM: http://marine.copernicus.eu/documents/PUM/CMEMS-WIND-PUM-012-002-005.pdf QUID: http://marine.copernicus.eu/documents/QUID/CMEMS-WIND-QUID-012-002-003-005.pdf

Winds blowing over the ocean induce sheared flows and waves that generate ocean turbulence. This turbulence transfers the momentum imparted by the winds down into the ocean and transports heat and constituents. In addition, ocean winds evaporate water and thus affect heat and mass fluxes and ocean salinity. Changing winds and associated air–sea interaction, currents and waves strongly affect the ocean state, both on global and local scales. Monitoring changes in ocean winds and stress on all spatial scales is therefore crucial to understand how changes in the ocean state (waves, currents, sea surface temperature, sea surface salinity, chlorophyll) are related to its atmospheric forcing. More in particular, Earth rotation causes the wind to generate the so-called Ekman ocean transport, which vertical component (pumping/suction) forces the Antarctic Circumpolar Current and ocean gyres through the wind stress curl.

In climate modelling and ocean applications ocean forcing is provided by atmospheric general circulation models. Although these models often use scatterometer observations as input, unresolved or poorly determined processes, such as wind dynamics or structure related to moist convection, the stable surface layer and atmospheric drag, cause both mean and variable errors in ocean wind forcing. Given the importance of model winds for this report on the ocean state, an assessment of the errors in atmospheric general circulation models forcing is provided with respect to the scatterometer observations.

Global monitoring of ocean mean winds, stress, its local variability and the associated Ekman pumping is introduced in this section. We provide a summary view of the current conditions and recent evolution in global sea surface winds from observational scatterometer data, highlighting major large-scale events in the context of climatology and trends, and exposing potential connections with the other ocean variables (such as waves, currents, sea surface temperature, sea surface salinity, chlorophyll) and global climate indicators (such as El Niño Southern Oscillation, North Atlantic Oscillation, Pacific Decadal Oscillation, Indian Ocean Dipole index, monsoons or tropical convection).

An approach to describing mean and variability of sea surface winds consists of resolving the field of motion into a time-mean component (called mean or steady wind, $\langle u \rangle$) and a time-variable component (called transient eddy wind, u') superposed upon it (Lorenz 1955) as:

$$u(t) = \langle u \rangle + u_s(t) + u'(t)$$

$$v(t) = \langle v \rangle + v_s(t) + v'(t)$$

where $u_s(t)$ is a seasonally dependent quantity representing the departure of the monthly mean from the annual mean wind, satisfying $\langle u_s(t) \rangle = 0$. The total wind kinetic energy is partitioned in mean, seasonal and transient eddy components as:

$$\mathrm{TKE} = \frac{1}{2}\langle u^2 + v^2 \rangle = \mathrm{MKE} + \mathrm{SKE} + \mathrm{TEKE}$$

$$\mathrm{MKE} = \frac{1}{2}(\langle u\rangle^2 + \langle v\rangle^2)$$

$$\mathrm{SKE} = \frac{1}{2}(\langle u_s^2\rangle + \langle v_s^2\rangle)$$

$$\mathrm{TEKE} = \frac{1}{2}(\langle u'^2\rangle + \langle v'^2\rangle)$$

In this section, the mean wind climatology is determined from the annual mean zonal and meridional wind components as

$$u_{\mathrm{mean}} = \langle u\rangle$$

$$v_{\mathrm{mean}} = \langle v\rangle$$

And the transient eddy wind climatology is determined as the square root of the annual mean variance of the zonal and meridional wind components around monthly means as

$$u_{\mathrm{eddy}} = \sqrt{\langle u'^2\rangle}$$

$$v_{\mathrm{eddy}} = \sqrt{\langle v'^2\rangle}$$

Accordingly, we show how the total wind kinetic energy is partitioned in mean and transient eddy components, since both affect ocean circulation and its gyres, the former through large-scale Ekman transport and upwelling/downwelling, the latter through vertical mixing via ocean eddies, surface and internal wave motions, etc. (Large et al. 1994). Aside from mean and transient wind statistics, this section introduces Ekman pumping as ocean-monitoring parameter. Ekman pumping is defined as $\mathrm{curl}(\tau/\rho_0 f)$ (Ekman 1905), and it relates to the curl of the wind stress vector, τ (de Kloe et al. 2017), scaled by a reference ocean density, ρ_0, and the Coriolis parameter f. As a rule of thumb, cyclonic winds will induce a net divergence in Ekman transport and upwelling, or Ekman suction, while anticyclonic winds will induce a net convergence and downwelling, or Ekman pumping.

In this chapter, the reference climatology is calculated over the period 2007–2014. The 2017 anomalies in mean wind, transient eddy wind and Ekman pumping are interpreted in the context of the 2007–2014 climatology and the 2007–2017 trend.

2.1.1. Global mean wind

The climatology, 2007–2017 trends and 2017 anomaly in the global mean sea surface winds are illustrated in Figure 2.1.1, with major features listed in Table 2.1.1. In the tropical Pacific, the 2007–2017 trend is dominated by a general shift from cold (La Niña) to warm (El Niño) Southern Oscillation conditions, with a gradual deceleration of easterlies in the central and western Tropical Pacific (Tag A1 in Figure 2.1.1(b)), along with enhanced easterlies and mean wind convergence in the eastern Pacific (Tag A2 in Figure 2.1.1(b)). 2017 is a year with a short or aborted warm El Niño Southern Oscillation event and a return to more neutral conditions, showing weak westerly anomalies in the western Tropical Pacific and a more easterly flow with reduced wind convergence in the eastern Tropical Pacific (Figure 2.1.1(c)), connected to cooling of sea surface temperatures in the central and eastern Tropical Pacific (cf. http://marine.copernicus.eu/science-learning/ocean-monitoring-indicators/). In the eastern Tropical Pacific, northwesterly wind anomalies are also associated with the onset of a 'Coastal El Niño' in 2017 (Tag A3 in Figure 2.1.1, cf. Section 4.7 of this report).

Connected to the gradually warmer El Niño Southern Oscillation conditions (reversed Walker Circulation) during the climatology period, the 2007–2017 mean wind trend is dominated by cyclonic anomalies over the North and South Pacific subtropical gyres (Tag B in Figure 2.1.1(b)). In line with the trend, the 2017 mean wind anomaly registers cyclonic anomalies over the Pacific subtropical gyres, together with a reduction of the Aleutian Sea Low in the North Pacific (Tag C), and an intensification of the South Pacific High (Tag D). Cyclonic anomalies in the North Pacific are associated with a weakening of the central and eastern branches of the North Pacific Gyre (cf. Section 2.7) and related to the Pacific Decadal Oscillation index, which projects onto a warm phase in 2017, connected with warm SST anomalies along the US Coast and cold SST anomalies across the northern Pacific (cf. Section 1.1.1).

The 2007–2017 mean wind trend in the Southern Ocean is dominated by a shift towards higher Southern Annular Mode indices (Thompson and Solomon 2002), corresponding to stronger-than-average westerlies over the mid-high latitudes (50S–70S, see Tag F in Figure 2.1.1(b)) and weaker westerlies in the mid-latitudes (30S–50S). The higher Southern Annular Mode indices have been associated with large but statistically insignificant meridional wind anomalies (northerly near the Antarctic Peninsula, Tag E1, and southerly in the Ross Sea, Tag E2) during the 1992–2010 period (Holland and Kwok 2012) suggesting that a deepening of the autumn Amundsen Sea Low is connected with the evolution of West-Antarctic climate and sea ice in the Pacific sector (Raphael et al. 2016). The variability and change of the Amundsen Sea Low remains complex (Turner et al. 2013), and it fails to provide a consistent deepening trend over the 2007–2014 period analysed here.

The 2007–2014 climatology over the Atlantic Ocean is dominated by a shift to higher North Atlantic Oscillation

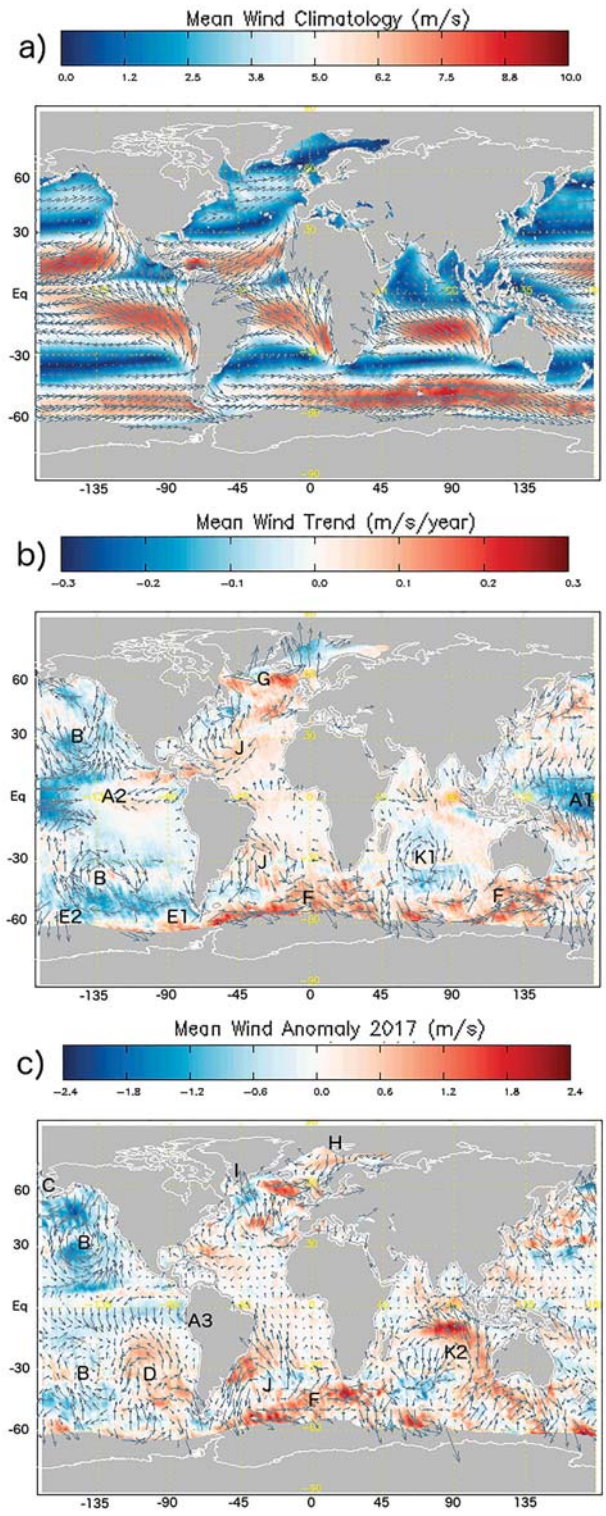

Figure 2.1.1. Global map of annual mean wind (product reference 2.1.1, ASCAT observations): 2007–2014 climatology (top), 2007–2017 decadal trend (middle, arrows at 95% significance level) and anomaly in 2017 relative to the climatology (bottom). Tagged features are listed in Table 2.1.1.

conditions, which are associated to increasing westerlies along the 55N–60N band (Tag G in Figure 2.1.1(b)). In line with the trend, the 2017 mean wind anomaly shows enhanced westerlies in the North Atlantic, accompanied by an enhancement of the Azores High and deepening of the Icelandic Low. In contrast to the general trend of increasing southerly meridional anomalies observed in the Greenland and Norwegian Seas, the 2017 anomaly shows enhanced subpolar north-easterlies (Tag H in Figure 2.1.1(c)). We also observe southeasterly wind anomalies in the Labrador Sea (Tag I in Figure 2.1.1(c)), weakening the local mean flow and connected to the weakening of the North Atlantic cold sea surface temperature anomaly as it is pushed further into the subpolar gyre (cf. Section 4.2). The 2007–2017 mean wind trend and anomalies are dominated by anticyclonic anomalies over the North and South Atlantic subtropical gyres (Tag J in Figure 2.1.1 (b)), with an intensification of the South Atlantic High near the Brazil-Malvinas Confluence, connected to unusually high sea surface temperatures in that region (http://marine.copernicus.eu/science-learning/ocean-monitoring-indicators) and associated with the Azores High near the Gulf Stream.

Finally, no significant trends are observed over the South Indian Ocean during the 2007–2017 period, except for a small cyclonic trend over the Mascarenes High off Madagascar (Tag K1 in Figure 2.1.1(b)). The 2017 mean wind anomaly is opposite to the trend, with a large anticyclonic anomaly over the South Indian gyre (Tag K2 in Figure 2.1.1(c)), enhancing the prevailing south-easterly trades and connected with unusually strong wind convergence off Sumatra. The enhanced south-easterly trades in the southern Indian Ocean are connected to colder than average sea surface temperatures on the eastern side, and warmer sea surface temperatures to the west (http://marine.copernicus.eu/science-learning/ocean-monitoring-indicators), also associated with the Indian Ocean Dipole Index, which projects into a positive phase in 2017.

2.1.2. Global transient eddy winds

The climatology, trends and 2017 anomaly in the global transient eddy winds are illustrated in Figure 2.1.2 below. Attending to their lower amplitude, we note that regional trends and anomalies in transient eddy winds are generally smaller than in the mean winds, indicating that most of the inter-annual variability in wind power is dominated by changes in persistent large-scale conditions, rather than changes in transient wind activity. We also note that trends and anomalies in transient wind are generally of opposite sign to trends and anomalies in the mean wind, indicating that changes in the mean wind are counterbalanced by changes in wind transience, which is reasonable when one considers that transient disturbances feed on the mean flow.

Table 2.1.1. Major features in global sea surface wind trends and anomalies, with associated ocean features as indicated in Figure 2.1.1.

TAG	Wind feature	Ocean feature
A1	El Niño Southern Oscillation trend: deceleration of easterlies in the central/western Tropical Pacific	Sustained extra-equatorial upwelling anomalies at latitudes from 3 to 7 deg.
A2	El Niño Southern Oscillation trend: enhanced easterlies and mean wind convergence in the eastern Pacific	Sustained extra-equatorial downwelling anomalies at latitudes from 3 to 7 deg.
A3	Coastal El Niño Southern Oscillation in 2017	Coastal circulation and production
B	Cyclonic anomalies over the North and South Pacific subtropical gyres	Upwelling trend and anomaly
C	Reduction of the Aleutian Sea Low	Downwelling anomaly Bering Strait
D	Intensification of the South Pacific High	Downwelling trend
E1	Deep Amundsen Sea Low anomalies: northerly near the Antarctic Peninsula	Ocean circulation and sea ice
E2	Deep Amundsen Sea Low anomalies: southerly in the Ross Sea	Ocean circulation and sea ice
F	Higher Southern Annular Mode	Northerly Ekman flow trend with associated down(up)welling to S(N)
G	Higher North Atlantic Oscillation conditions	Gulf Stream Dynamics
H	Increased subpolar north-easterlies in Greenland and Norwegian Seas	Enhanced ocean circulation/transport
I	Southeasterly wind anomalies in the Labrador Sea	Downwelling anomaly & trend off Newfoundland
J	Intensification of the Azores High and South Atlantic High	Atlantic Meridional Overturning
K1	Cyclonic trend over the Mascarenes High off Madagascar	Upwelling trend in Indian Ocean Gyre
K2	Anticyclonic anomaly in eastern tropical Indian Ocean	Positive phase of the Indian Ocean Dipole index

In connection with the trends in annual mean wind, we observe increasing wind variability over the central and western Tropical Pacific during the 2007–2017 period (Tag A1 in Figure 2.1.1 and Table 2.1.1), spatially correlated with the slowdown of trades and connected to the shift towards warmer El Niño Southern Oscillation conditions. Also note the localised regions of increased wind variability around Newfoundland and the Kamchatka Peninsula, both in the trends and the 2017 anomaly, and decreased wind variability over the Gulf of Alaska. We moreover observe a generally lower wind variability over the Southern Ocean (Tag F in Figure 2.1.1 and Table 2.1.1), in connection with a higher Southern Annular Mode – except in the Pacific sector. We also note a trend of increased wind variability over the subtropical Pacific gyres (Tag B in Figure 2.1.1 and Table 2.1.1) in connection with cyclonic anomalies in the mean winds, and lower wind variability in the eastern tropical Indian Ocean (Tag K2 in Figure 2.1.1 and Table 2.1.1) in 2017 connection with a strong anticyclonic anomaly in the mean wind.

Time series of globally averaged annual mean and eddy kinetic energy contributions for the 2007–2017 period split into zonal and meridional components for ASCAT observations and the ERA-Interim spatio-temporally interpolated collocations (product reference 2.1.1) have been computed (but not shown). It is interesting to compare the representation of the globally averaged wind kinetic energy provided by reanalyses to that of observations, since the accuracy of the former is limited by inhomogeneities introduced by changes in the observing system, as well as systematic errors inherited from the underlying model physics. Despite the regional trends noted earlier, there are no significant trends in globally averaged annual mean wind or wind variabilities over the 2007–2017 period. The partition of kinetic energy into mean and transient eddy components is however pictured somewhat differently in the ERA-Interim reanalysis, with a 6% higher mean wind energy and an 8% lower transient eddy wind energy than in the ASCAT measurements. The partition of mean wind energy into zonal and meridional components is also different in ERA-Interim, with stronger mean zonal winds and weaker meridional winds than in the ASCAT measurements, along with weaker zonal and meridional wind variabilities (not shown here, see Belmonte Rivas and Stoffelen 2019).

2.1.3. Ekman pumping

The climatology, trends and 2017 anomaly in Ekman upwelling are illustrated in Figure 2.1.3. We recall that trends and anomalies in Ekman suction/pumping, as derived from the curl of the wind stress vector, follow from the cyclonic/anticyclonic trends and anomalies in the annual mean wind. As an indication of large-scale vertical motions in the global oceans, ocean upwelling influences biological productivity (upwelling waters are usually rich in nutrients) and brings about changes in sea surface temperature that may affect weather and climate.

Due to their biological impact, a lot of research has focused on eastern boundary upwelling systems and their modes of variability, namely, the California and Peru-Humboldt systems, which are particularly impacted by El Niño Southern Oscillation; the Benguela system, which is affected by El-Niño-Southern-Oscillation-like variability and the Southern Annular Mode; or the Canary/Iberian system, which is impacted by the North Atlantic Oscillation and the Atlantic Multidecadal Oscillation (Bakun et al. 2015). Note that current scatterometer products lack data values closer than 25 km off the coast, as depicted in all figures. Some other

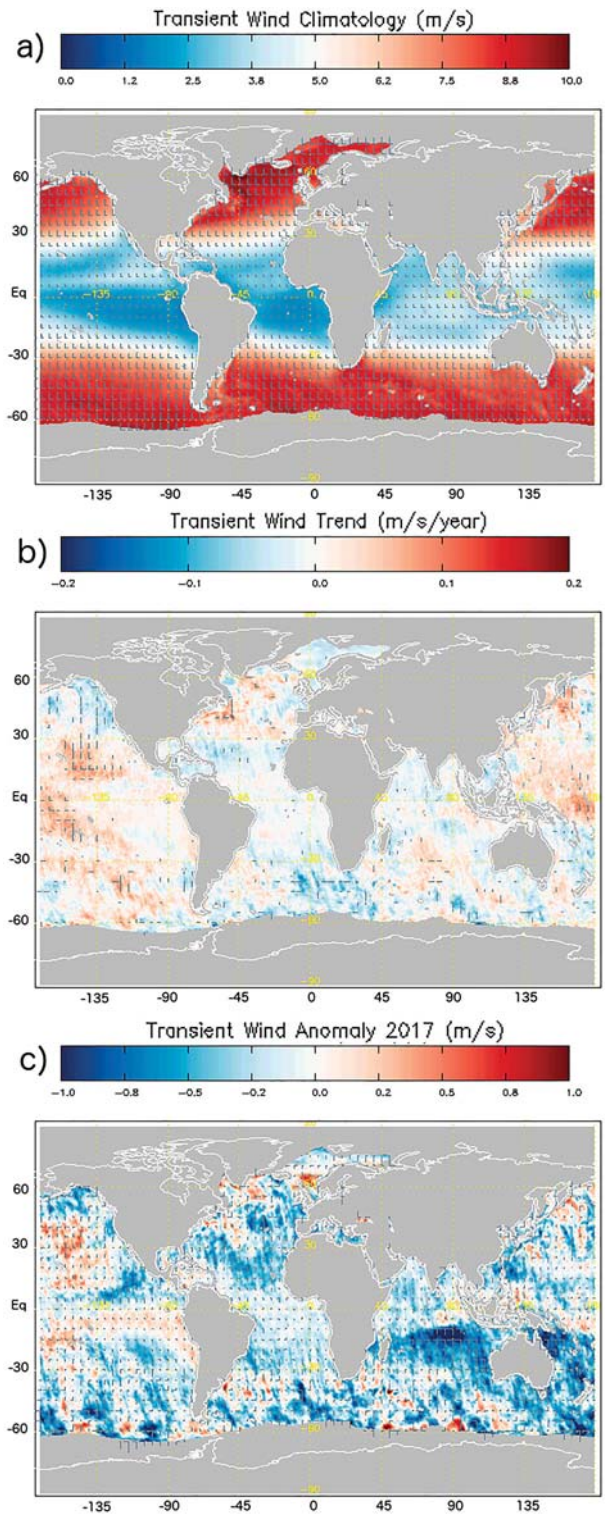

Figure 2.1.2. Global map of observed annual transient eddy wind (product reference 2.1.1, ASCAT observations): 2007–2014 climatology (top), 2007–2017 decadal trend (middle, arrows at 95% significance level) and anomaly in 2017 (bottom) with horizontal/vertical arrows showing the relative weight of the zonal/meridional components.

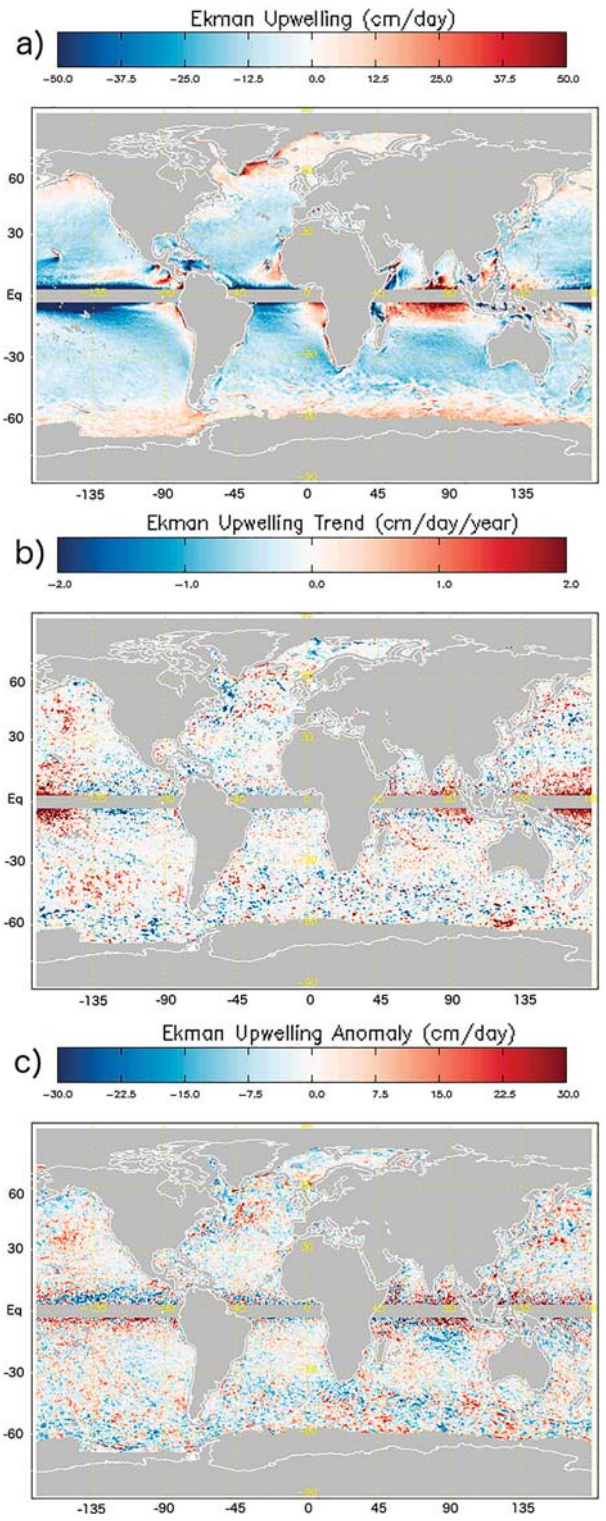

Figure 2.1.3. Global map of observed annual mean Ekman Upwelling (product reference 2.1.1, ASCAT observations): 2007–2014 climatology (top), 2007–2017 trend (middle, colours enhanced at 95% significance level) and anomaly in 2017 (bottom). Estimates between 5N and 5S are shaded as in (Risien and Chelton 2008) because the Coriolis force is small there.

researchers have focused on describing inter-annual variability in open-ocean upwelling.

In the tropical Pacific, we observe a persistent easterly flow that should create a thin tongue of upwelling cold water around the equator due to divergent Ekman transport approximately between 3S and 3N (within the shaded region in Figure 2.1.3). The trend of reduced easterlies in the central and western Tropical Pacific (associated to the general shift to warmer El Niño Southern Oscillation conditions during the 2007–2017 period) should result in downwelling anomalies (i.e. less upwelling) along the equatorial strip (Bograd and Lynn 2001), also within the shaded region in Figure 2.1.3. What we can see are the compensating downwelling zones North and South of the Equator (i.e. the extra-equatorial bands between 3 and 7 deg in both hemispheres) sustaining strong upwelling anomalies in the central and western Tropical Pacific (Tag A1 in Figure 2.1.1 and Table 2.1.1). These upwelling trends are indirectly related to reduced upwelling along the equatorial strip during the 2007–2017 period. In 2017, we still observe weak upwelling anomalies in the western extra-equatorial tropical Pacific, and somewhat more remarkable downwelling anomalies in the eastern extra-equatorial Pacific connected to enhanced easterlies there (Tag A2 in Figure 2.1.1 and Table 2.1.1).

Over the North and South Pacific Subtropical Gyres, we observe small upwelling trends and anomalies associated to persistent cyclonic anomalies in the mean wind (Tag B in Figure 2.1.1 and Table 2.1.1), along with a downwelling anomaly in the Bering Sea connected to the reduction of the Aleutian Sea Low (Tag C in Figure 2.1.1 and Table 2.1.1), and a downwelling anomaly (Tag D in Figure 2.1.1 and Table 2.1.1) connected with the intensification of the South Pacific High.

The strengthening of westerly winds over the Southern Ocean creates a band of enhanced northward Ekman flow with increased subpolar upwelling (trends and anomalies) to the south and enhanced downwelling to the north (Tag F in Figure 2.1.1 and Table 2.1.1) in connection with a stronger Southern Annular Mode (Hall and Visbeck 2002). In the Atlantic Ocean, we observe downwelling trends and anomalies off Newfoundland associated to a high pressure anomaly there (Tag I in Figure 2.1.1 and Table 2.1.1) (Spall and Pickart 2003), and upwelling trends and anomalies further east across the North Atlantic and around Iceland (Pelegri et al. 2006). Finally, we observe increased upwelling trends and anomalies in the eastern tropical Indian Ocean, which previous research has connected to Indian Ocean Dipole and El Niño Southern Oscillation conditions (Chen et al. 2016), along with a strong downwelling anomaly over the southern Indian Ocean connected to a large anticyclonic anomaly in the mean wind observed in 2017.

2.1.4. Concluding remarks

Wind, stress and Ekman variations are important in so far as they may be driving changes in other components (SST, SSS, sediment, biology) or initiate (local or remote) coupled processes that may push the climate system towards new states of equilibrium. Coupled processes, coastal processes, etc., have a host of relevant applications in economy and society. While these processes are best studied locally, we show that local changes, affecting ocean users, are strongly associated to changes in global atmospheric circulation. We moreover depict that the input used by most oceanographers suffers from large-scale forcing issues, in addition to the well-documented regional issues in processes and resolution. The associations between ocean indicators in other domains (sections) and the tagged features in this section's figures, appear a good way to connect the global atmospheric circulation changes to regional and local ocean circulation features and indicators. We also imply that for many of our users, the large-scale mean and transient errors in NWP forcing will be relevant in user applications, as it will provide errors in the time-dependent ocean response. It will be useful to further document and monitor these errors and the temporal changes in them. Finally, we note that efforts are ongoing to improve the coastal processing of scatterometer data, hence enhancing the usefulness of our products for ocean applications.

2.2. The seasonal intensification of the slope Iberian Poleward Current

Authors: Anna Rubio, Ivan Manso-Narvarte, Ainhoa Caballero, Lorenzo Corgnati, Carlo Mantovani, Emma Reyes, Annalisa Griffa and Julien Mader

Statement of main outcomes: The combination of surface HF radar data and data from ADCP moorings is showcased as a promising approach for the monitoring of the slope currents in the southeastern Bay of Biscay and the Iberian Poleward Current seasonal intensification. Persistent and intense eastward currents are observed during winter periods and affect the measured water column down to 150 m depth. During summer time, stronger vertical shear is observed, both during eastward and westward current events. Strong fluctuations occur in parallel to intense north-northwestern and southern wind changes in both seasons. This variability is expected to have a significant impact on the residence time and the water exchanges between the coast and the open ocean in the area.

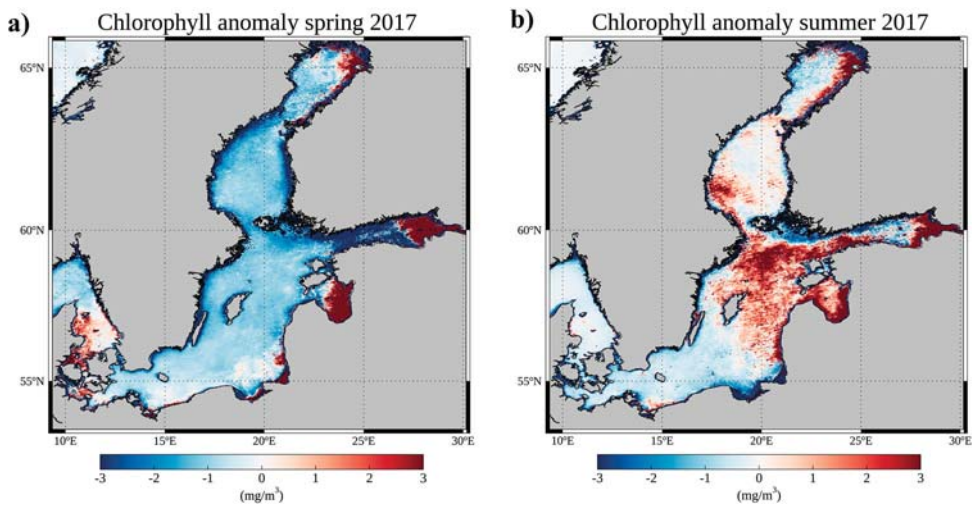

Figure 2.4.5. Chlorophyll-a anomaly fields in the Baltic Sea in spring 2017 relative to the 1998–2014 spring mean field (a) and in summer 2017 relative to the 1998–2014 summer mean field (b). Data from product reference 2.4.2.

matter could be a major contributor to the high attenuation coefficient values, elevated attenuation coefficient values are seen in the entire Baltic Proper and the Bothnian Sea. In spring 2017, attenuation coefficient anomaly is negative all over the Baltic Sea (Figure 2.4.4(c)). A very high positive attenuation coefficient anomaly in the southeastern Gulf of Riga and eastern Gulf of Finland could include contamination of attenuation coefficient values from ice coverage. The differences in the attenuation coefficient anomaly in the springs of 2016 and 2017 are well reflected in the spatiotemporal coverage of the spring bloom, with the 2017 spring bloom being less than half of the spring bloom in 2016 (Figure 2.4.2(a)). The attenuation coefficient anomaly in summer 2016 is higher than in 2017 (Figure 2.4.4(b,d)), which is reflected also in the summer mean attenuation coefficient values (Figure 2.4.3) and in the spatiotemporal coverage of subsurface bloom, but not in the surface bloom (Figure 2.4.2(b)). Measured phytoplankton wet weight during spring bloom has been substantially higher in 2016 than in 2017, but comparable in the summers of 2016 and 2017 (Wasmund et al. 2017, 2018). In general, by comparing time series of summer mean attenuation coefficient values and summer bloom spatiotemporal coverage (Figures 2.4.2(b) and 2.4.3), we conclude no obvious match of these two parameters.

Chlorophyll-a spring anomaly in 2017 showed high values in the Gulf of Riga and the eastern part of the Gulf of Finland. High values with a smaller extent were visible in the northern coastal area of the Bothnian Bay and coastal areas of the Gulf of Gdansk and the Curonian Lagoon. To a larger extent, lower values are evident in the western part of the Gulf of Finland. The spatial distributions of measured chlorophyll-a are versatile in the spring of 2017 (Wasmund et al. 2018). In March, chlorophyll-a concentrations show higher values near the Danish Straits, with decreasing gradient towards the Gotland Basin. In May, the spatial gradient of chlorophyll-a was reversed – chlorophyll-a concentrations were significantly higher in the eastern and southern Gotland basin and lower near the Danish Straits.

Chlorophyll-a summer anomaly in 2017 has highest values in the eastern part of the Gulf of Finland and the Gulf of Riga, which extend further in space, compared to same areas in 2016 (Raudsepp et al. 2018). Extensive high chlorophyll-a values in the northern Baltic Proper in 2017 are not visible in 2016. At the same time, high chlorophyll-a values, which are seen across the Bothnian Bay in 2016, are only limited to the eastern coast in 2017. Both years share similarly low summer chlorophyll-a anomaly values in the Gulf of Gdansk and on the coasts of Lithuania and Kaliningrad, except for the outflow area from Curonian lagoon. In summer 2017, spatial differences in measured chlorophyll-a concentrations were relatively uniform in the southern Baltic, but much higher in the Eastern Gotland basin (Wasmund et al. 2018).

2.5. Cod reproductive volume potential in the Baltic Sea

Authors: Urmas Raudsepp, Ilja Maljutenko, Mariliis Kõuts

Statement of outcome: Cod (*Gadus morhua*) is a characteristic fish species in the Baltic Sea with major economic importance. The Baltic cod stocks have

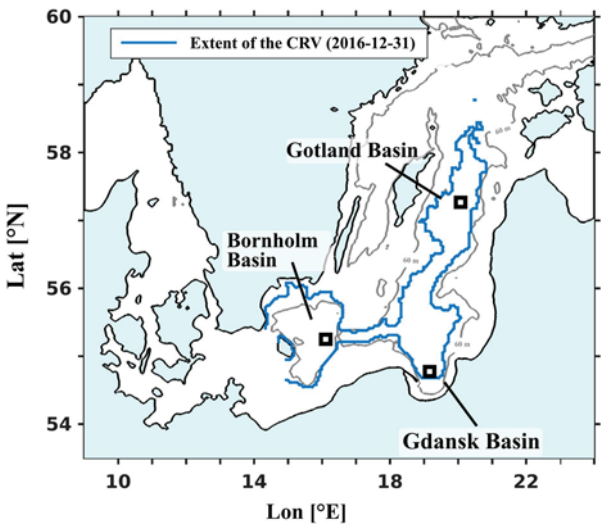

Figure 2.5.1. Map of the Southern Baltic Sea showing locations of the basins. Sixty metre isodepth is marked with grey line. Blue contour show geographical extent of cod reproductive volume (CRV) for 2016-12-31 based on CMEMS product reference 2.5.1 and 2.5.2.

gone through a steep decline in the late 1980s (ICES 2016). In this section we focus on the impact of the Major Baltic Inflows on the eastern cod population. Hydrographic conditions affect cod directly through the survival of eggs. Our results indicate that the water volume with suitable conditions for cod reproduction has stayed mostly on the same level during the period of 1993–2017. We verify the importance of the Major Baltic Inflows shaping a suitable environment for cod reproduction and the Bornholm basin as the most important spawning ground. Cod reproductive volume is on a relatively stable level in the Bornholm basin, while highly dependent on inflows in the downstream basins. Available data about the Major Baltic Inflows can be used as an indicator of important biological processes.

Products used:

Ref. No.	Product name and type	Documentation
2.5.1	BALTICSEA_REANALYSIS_PHY_003_011 Reanalysis	PUM: http://marine.copernicus.eu/documents/PUM/CMEMS-BAL-PUM-003-011.pdf QUID: http://marine.copernicus.eu/documents/QUID/CMEMS-BAL-QUID-003-011.pdf
2.5.2	BALTICSEA_REANALYSIS_PHY_003_012 Reanalysis	PUM: http://marine.copernicus.eu/documents/PUM/CMEMS-BAL-PUM-003-012.pdf QUID: http://marine.copernicus.eu/documents/QUID/CMEMS-BAL-QUID-003-012.pdf

Atlantic cod (*Gadus morhua*) is a major fish species of the Baltic Sea with high economic importance. The Baltic Sea cod consists of two genetically different populations – eastern and western Baltic cod. We focus on the eastern cod as it contributes to the landing numbers the most and has several spawning grounds in the deep areas of the Baltic Sea, east of Bornholm island. The eastern Baltic cod stock has been at the absolute low since the 1980s (ICES 2005; FishSource). There are two sets of governing factors – anthropogenic and natural. Anthropogenic effects mostly manifest through high fishing pressure. Natural conditions vary in the Baltic Sea in relation to water exchange with the North Sea – the Major Baltic Inflows in particular, which create the specific environmental conditions for cod to reproduce. We focus on the Major Baltic Inflows, the most important controlling factor of cod recruitment in the Baltic Sea (MacKenzie et al. 1996; Köster et al. 2005). The dramatic decline of cod stocks overlaps with the decrease in the frequency and intensity of the North Sea advections in the late 1980s (Heikinheimo 2008). Recruitment started to decline in the mid-1980s despite the spawning stock and the number of eggs produced by old females still being high (Cardinale and Arrhenius 2000). There was no significant change in fishing pressure during that period (ICES 2005). This implies that other factors besides fishing might have been important (Heikinheimo 2008). Hydrographic factors affect cod recruitment directly through the survival of eggs, and indirectly via species composition and availability of the prey organisms which are essential for cod larvae survival (Heikinheimo 2008). As a result, cod reproduction in the eastern areas of the sea, including the Gdansk Deep, almost completely ceased and continued only in the Bornholm Basin (Nielsen 1998). Karasiova (2011) found a positive correlation between the interannual fluctuations of egg production and water volumes with conditions favourable for cod reproduction in the four main spawning areas in the Baltic Sea.

The Bornholm Basin is the most important spawning ground for the eastern Baltic cod stock, followed by the Gotland and Gdansk basins (MacKenzie et al. 1996; Hinrichsen et al. 2017) (Figure 2.5.1). In order to describe the relationship between cod reproduction and the Major Baltic Inflows we use 'cod reproductive volume' (CRV), which is based on previous research and takes into account the three most important influencing factors of cod reproductive success: salinity over 11 g/kg (product reference 2.5.1), oxygen content > 2 ml/l (product reference 2.5.2) and water temperature over 1.5°C (product reference 2.5.1) (MacKenzie et al. 1996; Heikinheimo 2008; Plikshs

et al. 2015). Our aim is to derive the reproductive potential of the eastern Baltic cod from dynamics, characteristics and volume of the inflowing water and compare these results with the published numbers. This approach enables to use available data about Major Baltic Inflows as an indicator for important biological processes, which could be of use in evaluating the status and development of Baltic cod stocks in the future. The boundary of the Baltic Sea has been taken from the western boundary of the Bornholm Basin according to the ICES fishery subdivisions.

Our results show that the cod reproductive volume has been more or less stable in the Bornholm Basin during the period of 1993–2017 (Figure 2.5.2(a)). There were periods of elevated cod reproductive volume in the Baltic Sea in 2003–2004, 2006–first half of the 2007, 2014–first half of the 2015 and 2016, which contribute to a small positive trend of 8.8 km^3/year over the study period. Saline water volume of the Baltic Sea, however, shows considerable increase since the 1993 Major Baltic Inflow (Figure 2.5.2(a)) and due to the following inflows in 1997, 2003 and 2014. Cod biomass values were estimated to be slightly higher around 2010, which might reflect the period with sufficient conditions after 2003 (Karasiova 2011). This is in an agreement with the highest values of cod stock size indicator (Figure 2.5.2(a)). The ICES stock size indicator is a combined biomass index, in kg/h, of cod ≥30 cm from the Baltic International Trawl Survey (BITS) in quarters 1 and 4 in the Baltic Sea subdivisions of 25–28 (ICES 2018). Also, egg counts responded to Major Baltic Inflows with higher values in 1994, 1997 and 2003 (Karasiova 2011). The cod reproductive volume is in minimum in 2000 and in 2011 with the values comparable to low cod reproductive volume values at the end of the stagnation period in the Baltic. The saline water volume has never dropped to a value comparable to the value at the end of the stagnation period. The lowest saline water volume values can be seen in the Baltic Sea in 2002 and 2013.

There is a strong positive correlation between cod reproductive volume and saline water volume in the Bornholm Basin ($R^2 = 0.82$) and the two volumes vary less compared to the rest of the Baltic Sea (Figure 2.5.2(a)). In the Bornholm Basin, average saline water volume and cod reproductive volume are 315 km^3 (SD = 59 km^3) and 220 km^3 (SD = 80 km^3), respectively. In the rest of the Baltic Sea, the saline water volume is associated with Major Baltic Inflows – the larger the inflow, the bigger the volume of salty water that goes to other basins. The impact of the inflow events was bigger following the inflows of

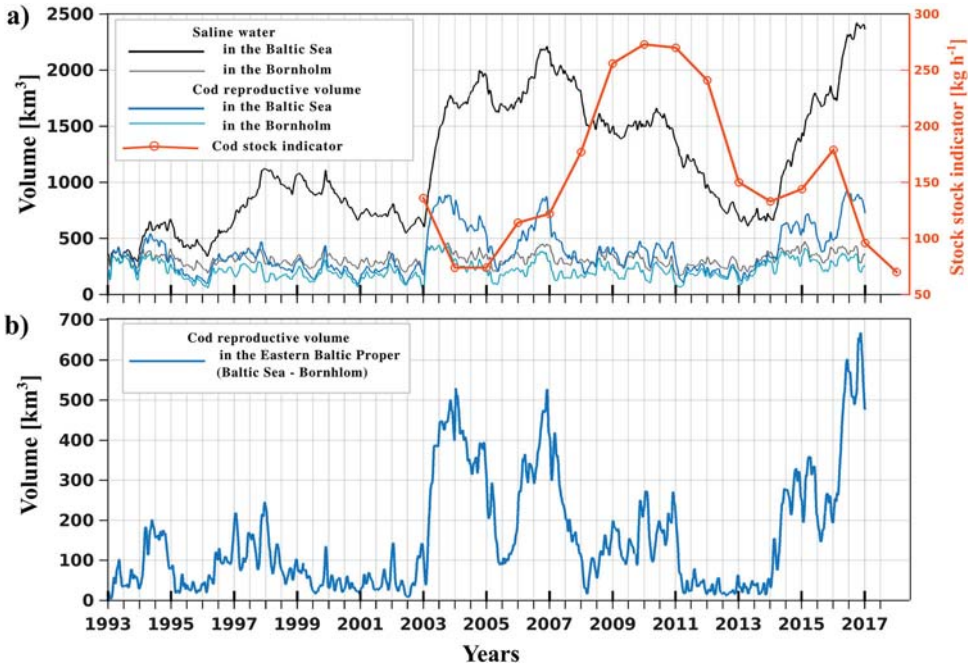

Figure 2.5.2. (a) Time series of saline water volumes (SWV, S > 11 g/kg) black line and cod reproductive volumes (CRV) in the Baltic Proper (thick lines), excluding Arkona Basin; and in Bornholm Basin (thin lines); and cod stock size indicator. Dots in the red line represent the geometric mean of the biomass of ≥30 cod specimens in the previous year from the Baltic International Trawl Survey in subdivisions 25–28. (b) Time series of cod reproductive volume (CRV, S > 11 g/kg, O_2 > 2 ml/l) extending outside the Bornholm Basin. Time series are calculated from CMEMS product reference 2.5.1 and 2.5.2.

2003 and 2014. Similarly to salinity, increase in cod reproductive volume reflects the impact of the Major Baltic Inflows to the basins downstream of the Bornholm Basin (Figure 2.5.2(a,b)). Suitable conditions for cod reproduction persist for a shorter time period (Figure 2.5.2(b)) than that of the saline water volume (Figure 2.5.2(a)) which means that oxygen content declines faster than salinity in the bottom layers of the Baltic Sea (Raudsepp et al. 2018).

The effect of the Major Baltic Inflows on cod reproduction has been studied earlier and results indicate that the effect can be small to important based on the pre-existing hydrological conditions, which determine how big the potential spawning area will be. The inflow of 1993–1995 had a small effect because the conditions before did not predispose the formation of large spawning areas, while the effect of the Major Baltic Inflow in 2003 was bigger (Karaseva and Zezera 2016). We used data from ICES to compare our values with the stock size indicator. The data fits our model results with increased cod reproductive volume having a positive effect on cod reproduction success, which reflects in an increase of stock size indicator ca. 4–5 years after the Major Baltic Inflow. The inflow in 2003 resulted in an increased stock size between 2007 and 2012 (Figure 2.5.2(a)). Eastern Baltic cod reaches maturity around age 2–3, depending on the population density and environmental conditions. Lack of oxygen and low salinity cause stress, which negatively affects cod recruitment, whereas sufficient conditions may bring about male cod maturation even at the age of 1.5 years (Cardinale and Modin 1999; Karasiova et al. 2008). Since there was a Major Baltic Inflow again in 2014, which increased the cod reproductive volume up to 900 km^3 in the Baltic Sea (Figure 2.5.2(a)), we expect an increase of cod stock size starting from 2018–2019.

2.6. The North Pacific Gyre Oscillation

Authors: Benoît Tranchant, Isabelle Pujol, Emanuele Di Lorenzo, Jean-François Legeais

Statement of main outcome: The North Pacific Gyre Oscillation is defined as the second dominant mode of variability of SSH anomaly and SST anomaly in the North East Pacific. This mode emerges as the leading mode of decadal variability for surface salinity and upper ocean nutrients, and is in a negative phase since 2014. This condition reflects a reduced amplitude of the central and eastern branches of the North Pacific gyre, corresponding to a reduced coastal upwelling and thus a lower sea surface salinity and concentration of nutrients. Here, this indicator is inferred from a long time series of SSH anomalies over the North East Pacific (25°–62°N, 180°–250°E) and will be regularly updated.

Product used:

Ref. No.	Product name and type	Documentation
2.6.1	SSH anomalies Numerical Ocean Model	Di Lorenzo et al. (2008)
2.6.2	SSS anomalies Observations	Scripps Pier measurements collected by the Birch Aquarium at Scripps staff and volunteers. Data provided by the Shore Stations Program sponsored at Scripps Institution of Oceanography by California State Parks, Division of Boating and Waterways. Contact: shorestation@ucsd.edu.
2.6.3	NCEP wind stress 1950–2004 Numerical Atmospheric Model	The NCEP/NCAR 40-Year Reanalysis Project (Kalnay et al. 1996)
2.6.4	Altimeter data: previous version of SEALEVEL_GLO_PHY_L4_REP_OBSERVATIONS_008_047 (see below) Remote sensing	Product User Manual (CMEMS-SL-PUM-008-032-051) http://marine.copernicus.eu/documents/PUM/CMEMS-SL-PUM-008-032-051.pdf Quality Information Document (CMEMS-SL-QUID-008-032-051) http://marine.copernicus.eu/documents/QUID/CMEMS-SL-QUID-008-032-051.pdf
2.6.5	SEALEVEL_GLO_PHY_L4_REP_OBSERVATIONS_008_047 Remote sensing	Product User Manual (CMEMS-SL-PUM-008-032-051) http://marine.copernicus.eu/documents/PUM/CMEMS-SL-PUM-008-032-051.pdf Quality Information Document (CMEMS-SL-QUID-008-032-051) http://marine.copernicus.eu/documents/QUID/CMEMS-SL-QUID-008-032-051.pdf
2.6.6	SEALEVEL_GLO_PHY_L4_REP_OBSERVATIONS_008_046 Remote sensing	Product User Manual (CMEMS-SL-PUM-008-032-051) http://marine.copernicus.eu/documents/PUM/CMEMS-SL-PUM-008-032-051.pdf Quality Information Document (CMEMS-SL-QUID-008-032-051) http://marine.copernicus.eu/documents/QUID/CMEMS-SL-QUID-008-032-051.pdf

The Decadal North Pacific Gyre Oscillation is a climate pattern defined by Di Lorenzo et al. (2008). The North Pacific Gyre Oscillation term is used because its

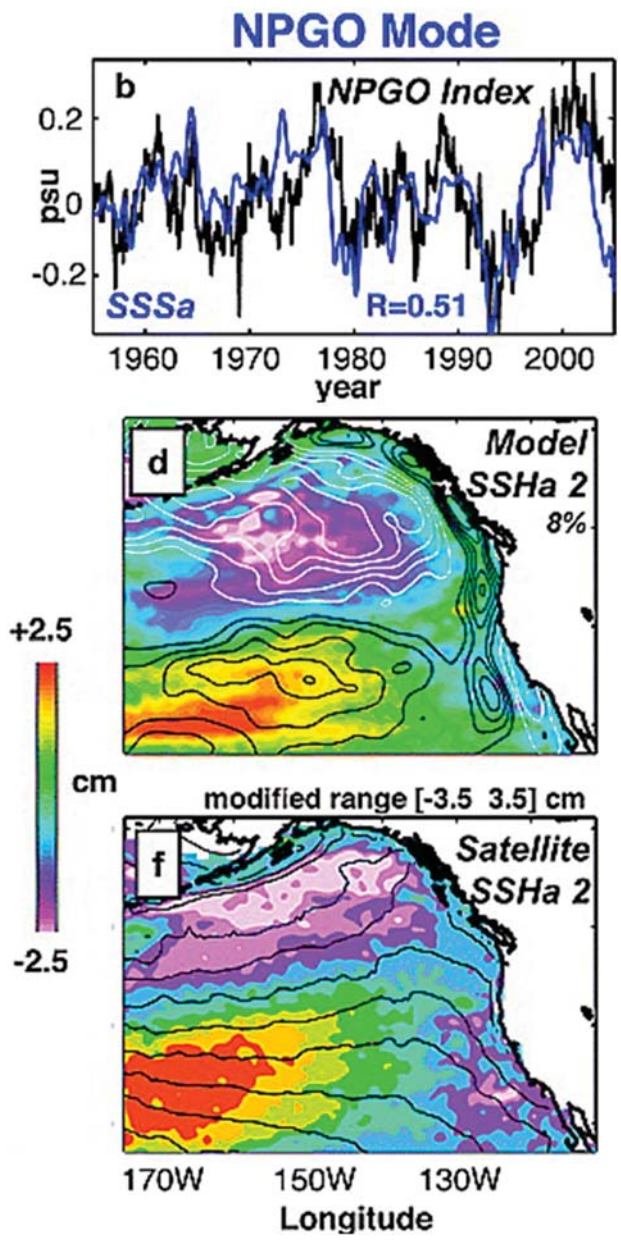

Figure 2.6.1. (b) Time series of La Jolla Scripps Pier SSSa (reference product 2.6.2) (blue) compared to the NPGO index (correlation $R = 0.51$, 99% significance), defined as the second PC of model SSHa (black). The SSSa records are detrended and a 12 months running mean is applied. (d) Regression maps of model NPGO indices with the model SSHa. The white (black) contours indicate regions of positive (negative) wind stress curl (Ekman upwelling) as inferred from a regression of the model PCs with the NCEP wind stress curl (reference product 2.6.3). The % variance accounted for by each regression map is indicated. (f) Regression maps of the model NPGO index with satellite altimeter data gathered between 1993 and 2004 (reference product 2.6.4). The colour range is modified to [3.5 3.5] in Figure 2(f) to properly display the map (black contours are satellite/drifter-derived mean dynamic height [Niiler et al. 2003]). Credit from Di Lorenzo et al. (2008).

fluctuations reflect changes in the intensity of the central and eastern branches of the North Pacific gyre circulations. Thus, it has been defined as the 2nd dominant mode of sea surface height variability in the Northeast Pacific (25°–62°N, 180°–250°E, see Figure 2.6.1(d,f)). The North Pacific Gyre Oscillation index has been defined as the second Principal Component of model Sea Surface Height anomaly calculated over the period 1950–2004 (reference product 2.6.1), see Figure 2.6.1(b). Di Lorenzo et al. (2008) suggest that the North Pacific Gyre Oscillation is the oceanic expression of the atmospheric North Pacific Oscillation (Walker and Bliss 1932). This seems reinforced by the recent work of Yi et al. (2018) that show consistent pattern feature between the atmospheric North Pacific Oscillation and the oceanic North Pacific Gyre Oscillation.

This index measures change in the North Pacific gyres circulation and explains key physical-biological ocean variables including temperature, salinity, sea level, nutrients, chlorophyll-a. One example is the coherent variation of model and observed/modelled SSS (Sea Surface Salinity) in the Northeast Pacific (Di Lorenzo et al. 2008), see Figure 2.6.1(b). Like the Pacific decadal oscillation, the North Pacific Gyre Oscillation is a basin-scale feature and captures prominent low-frequency changes in the Pacific physical and biological fields. This is why the North Pacific Gyre Oscillation index provides a strong indicator of fluctuations in the mechanisms driving planktonic ecosystem dynamics.

A positive North Pacific Gyre Oscillation phase is a dipole pattern with negative SSH anomaly north of 40° N and the opposite south of 40°N. The North Pacific Gyre Oscillation index is presently in a negative phase, associated with a positive SSH anomaly north of 40°N and negative south of 40°N. This reflects a reduced amplitude of the central and eastern branches of the North Pacific gyre, corresponding to a reduced coastal upwelling and thus a lower sea surface salinity and concentration of nutrients.

The EOF's amplitude pattern (pers. Comm. Di Lorenzo) has been inferred from the principal component analysis. This regression map of the model North Pacific Gyre Oscillation index is used/projected with normalised satellite altimeter delayed-time sea level anomalies to calculate and update the NPGO index. An example is given on Figure 2.6.2 where the NPGO index has been projected on the last version of the reprocessed altimeter sea level record (CMEMS reference product 2.6.5).

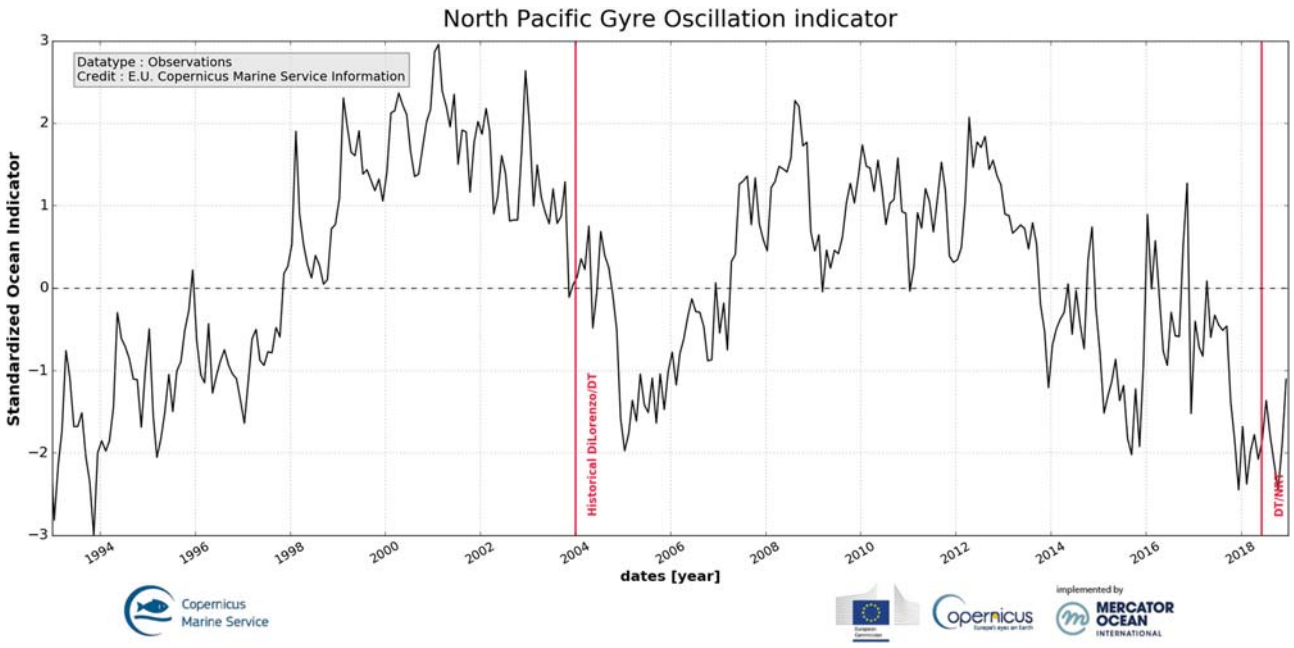

Figure 2.6.2. NPGO index monthly averages. From 1993 to 2003, the NPGO index is calculated from ref. 2.6.4, see Di Lorenzo et al. (2008). From 2004 onward, the NPGO index has been projected on normalised satellite altimeter Delayed-Time (DT) (CMEMS reference product 2.6.5) and Near-Real-Time (NRT) (CMEMS reference product 2.6.6).

2.7. Sea level, sea surface temperature and SWH extreme percentiles: combined analysis from model results and in situ *observations*

Authors: Enrique Álvarez Fanjul, Álvaro de Pascual Collar, Begoña Pérez Gómez, Marta De Alfonso, Marcos García Sotillo, Joanna Staneva, Emanuela Clementi, Alessandro Grandi, Anna Zacharioudaki, Gerasimos Korres, Michalis Ravdas, Richard Renshaw, Jonathan Tinker, Urmas Raudsepp, Priidik Lagemaa, Ilja Maljutenko, Gerhard Geyer, Malte Müller, Veli Çağlar Yumruktepe

Statement of main outcome: This section explores the temporal and spatial variability of the extremes of sea level, waves and sea surface temperature over European seas and the Arctic region. The analysis combines information from both in-situ observations and model data available through CMEMS, demonstrating the potential of the service and the benefits of merging observational and modelled products. The main outcomes of this joint analysis of anomalies in 2017 relative to long-term average conditions include: (i) sea level extremes variability was near average in all coastal areas of Europe and the Arctic except for a few stations in the UK, west of Normandy and the northwestern Gulf of Bothnia in the Baltic, (ii) wave extremes were larger than usual in most of the Iberia-Biscay-Ireland region (anomalies of significant wave height about +0.5 m) and in the western Mediterranean Sea (+0.75 m) and lower than usual in the eastern Mediterranean and near the Irish coast (−0.5 m). In the Black Sea, the usual spatial pattern is inverted, being the largest extremes on the eastern and central areas (up to 0.7 m). (iii) Sea surface temperature extremes anomalies were strongly positive in most of the Mediterranean Sea, typically by +1°C, and in the Northern Arctic regions reaching as high as +6°C. Negative anomalies were found in the Baltic (up to −3°C) and the North Sea (∼−1°C).

Products used:

Ref. No.	Product name and type	Documentation
2.7.1	INSITU_IBI_TS_REP_OBSERVATIONS_013_040 Observations reprocessed	PUM: http://marine.copernicus.eu/documents/PUM/CMEMS-INS-PUM-013.pdf QUID: http://marine.copernicus.eu/documents/QUID/CMEMS-INS-QUID-013-040.pdf
2.7.2	INSITU_NWS_TS_REP_OBSERVATIONS_013_043 Observations reprocessed	PUM: http://marine.copernicus.eu/documents/PUM/CMEMS-INS-PUM-013.pdf QUID: http://marine.copernicus.eu/documents/QUID/CMEMS-INS-QUID-013-043.pdf
2.7.3	INSITU_MED_TS_REP_OBSERVATIONS_013_041 Observations reprocessed	PUM: http://marine.copernicus.eu/documents/PUM/CMEMS-INS-PUM-013.pdf QUID: http://marine.copernicus.eu/documents/QUID/CMEMS-INS-QUID-013-041.pdf
2.7.4	INSITU_BAL_TS_REP_OBSERVATIONS_013_038 Observations reprocessed	PUM: http://marine.copernicus.eu/documents/PUM/CMEMS-INS-PUM-013.pdf QUID: http://marine.copernicus.eu/documents/QUID/CMEMS-INS-QUID-013-038.pdf

(*Continued*)

Continued.

Ref. No.	Product name and type	Documentation
2.7.5	INSITU_IBI_NRT_OBSERVATIONS_013_033 Observations	PUM: http://marine.copernicus.eu/documents/PUM/CMEMS-INS-PUM-013.pdf QUID: http://marine.copernicus.eu/documents/QUID/CMEMS-INS-QUID-013-030-036.pdf
2.7.6	INSITU_NWS_NRT_OBSERVATIONS_013_036 Observations	PUM: http://marine.copernicus.eu/documents/PUM/CMEMS-INS-PUM-013.pdf QUID: http://marine.copernicus.eu/documents/QUID/CMEMS-INS-QUID-013-030-036.pdf
2.7.7	INSITU_MED_NRT_OBSERVATIONS_013_035 Observations	PUM: http://marine.copernicus.eu/documents/PUM/CMEMS-INS-PUM-013.pdf QUID: http://marine.copernicus.eu/documents/QUID/CMEMS-INS-QUID-013-030-036.pdf
2.7.8	INSITU_BAL_NRT_OBSERVATIONS_013_032 Observations	PUM: http://marine.copernicus.eu/documents/PUM/CMEMS-INS-PUM-013.pdf QUID: http://marine.copernicus.eu/documents/QUID/CMEMS-INS-QUID-013-030-036.pdf
2.7.9	INSITU_GLO_NRT_OBSERVATIONS_013_030 Observations	PUM: http://marine.copernicus.eu/documents/PUM/CMEMS-INS-PUM-013.pdf QUID: http://marine.copernicus.eu/documents/QUID/CMEMS-INS-QUID-013-030-036.pdf
2.7.10	IBI_REANALYSIS_PHYS_005_002 Model reanalysis	PUM: http://marine.copernicus.eu/documents/PUM/CMEMS-IBI-PUM-005-002.pdf QUID: http://marine.copernicus.eu/documents/QUID/CMEMS-IBI-QUID-005-002.pdf
2.7.11	IBI_ANALYSIS_FORECAST_WAV_005_005 Model analysis	PUM: http://marine.copernicus.eu/documents/PUM/CMEMS-IBI-PUM-005-005.pdf QUID: http://marine.copernicus.eu/documents/QUID/CMEMS-IBI-QUID-005-005.pdf
2.7.12	IBI_ANALYSIS_FORECAST_PHYS_005_001 Model analysis	PUM: http://marine.copernicus.eu/documents/PUM/CMEMS-IBI-PUM-005-001.pdf QUID: http://marine.copernicus.eu/documents/QUID/CMEMS-IBI-QUID-005-001.pdf
2.7.13	BLKSEA_ANALYSIS_FORECAST_WAV_007_003 Model analysis	PUM: http://marine.copernicus.eu/documents/PUM/CMEMS-BS-PUM-007-003.pdf QUID: http://marine.copernicus.eu/documents/QUID/CMEMS-BS-QUID-007-003.pdf
2.7.14	BLKSEA_REANALYSIS_WAV_007_006 Model reanalysis	PUM: http://marine.copernicus.eu/documents/QUID/CMEMS-BS-QUID-007-006.pdf QUID: http://marine.copernicus.eu/documents/PUM/CMEMS-BS-PUM-007-006.pdf
2.7.15	MEDSEA_REANALYSIS_PHYS_006_004 Model reanalysis	PUM: http://marine.copernicus.eu/documents/PUM/CMEMS-MED-PUM-006-004.pdf QUID: http://marine.copernicus.eu/documents/QUID/CMEMS-MED-QUID-006-004.pdf DOI: https://doi.org/10.25423/medsea_reanalysis_phys_006_004, Simoncelli et al. (2014)
2.7.16	MEDSEA_HINDCAST_WAV_006_012 (period 2006–2017) Model hindcast	PUM: http://marine.copernicus.eu/documents/PUM/CMEMS-MED-PUM-006-012.pdf QUID: http://marine.copernicus.eu/documents/QUID/CMEMS-MED-QUID-006-012.pdf
2.7.17	NORTHWESTSHELF_ANALYSIS_FORECAST_PHYS_004_001_b Model analysis	PUM: http://marine.copernicus.eu/documents/PUM/CMEMS-NWS-PUM-004-001.pdf QUID: http://marine.copernicus.eu/documents/QUID/CMEMS-NWS-QUID-004-001-b.pdf
2.7.18	NORTHWESTSHELF_REANALYSIS_PHYS_004_009 Model reanalysis	PUM: http://marine.copernicus.eu/documents/PUM/CMEMS-NWS-PUM-004-009-011.pdf QUID: http://marine.copernicus.eu/documents/QUID/CMEMS-NWS-QUID-004-009-011.pdf
2.7.19	BALTICSEA_ANALYSIS_FORECAST_PHY_003_006 Model analysis	PUM: http://marine.copernicus.eu/documents/QUID/CMEMS-BAL-QUID-003-006.pdf QUID: http://marine.copernicus.eu/documents/PUM/CMEMS-BAL-PUM-003-006.pdf
2.7.20	BALTICSEA_REANALYSIS_PHY_003_011 Model reanalysis	PUM: http://marine.copernicus.eu/documents/PUM/CMEMS-BAL-PUM-003-011.pdf QUID: http://marine.copernicus.eu/documents/QUID/CMEMS-BAL-QUID-003-011.pdf
2.7.21	BALTICSEA_ANALYSIS_FORECAST_WAV_003_010 Model analysis	PUM: http://marine.copernicus.eu/documents/PUM/CMEMS-BAL-PUM-003-010.pdf QUID: http://marine.copernicus.eu/documents/QUID/CMEMS-BAL-QUID-003-010.pdf
2.7.22	IBI_REANALYSIS_WAV_005_006 Model reanalysis	PUM: http://marine.copernicus.eu/documents/PUM/CMEMS-IBI-PUM-005-006.pdf QUID: http://marine.copernicus.eu/documents/QUID/CMEMS-IBI-QUID-005-006.pdf
2.7.23	MEDSEA_ANALYSIS_FORECAST_PHY_006_013 Model analysis	PUM: http://marine.copernicus.eu/documents/PUM/CMEMS-MED-PUM-006-013.pdf QUID: http://marine.copernicus.eu/documents/QUID/CMEMS-MED-QUID-006-013.pdf
2.7.24	MEDSEA_ANALYSIS_FORECAST_WAV_006_017 Model analysis	PUM: http://marine.copernicus.eu/documents/PUM/CMEMS-MED-PUM-006-017.pdf QUID: http://marine.copernicus.eu/documents/QUID/CMEMS-MED-QUID-006-017.pdf
2.10.21	ARCTIC_ANALYSIS_FORECAST_PHYS_002_001_a Model analysis	PUM: http://marine.copernicus.eu/documents/PUM/CMEMS-ARC-PUM-002-ALL.pdf QUID: http://marine.copernicus.eu/documents/QUID/CMEMS-ARC-QUID-002-001a.pdf
2.10.22	ARCTIC_REANALYSIS_PHYS_002_003 Model reanalysis	PUM: http://marine.copernicus.eu/documents/PUM/CMEMS-ARC-PUM-002-ALL.pdf QUID: http://marine.copernicus.eu/documents/QUID/CMEMS-ARC-QUID-002-003.pdf

The first step of the methodology employed is to compute the 99th mean annual percentile for each Essential Ocean Variables, and for both observations and models. This is calculated as the mean of the 99th percentile from

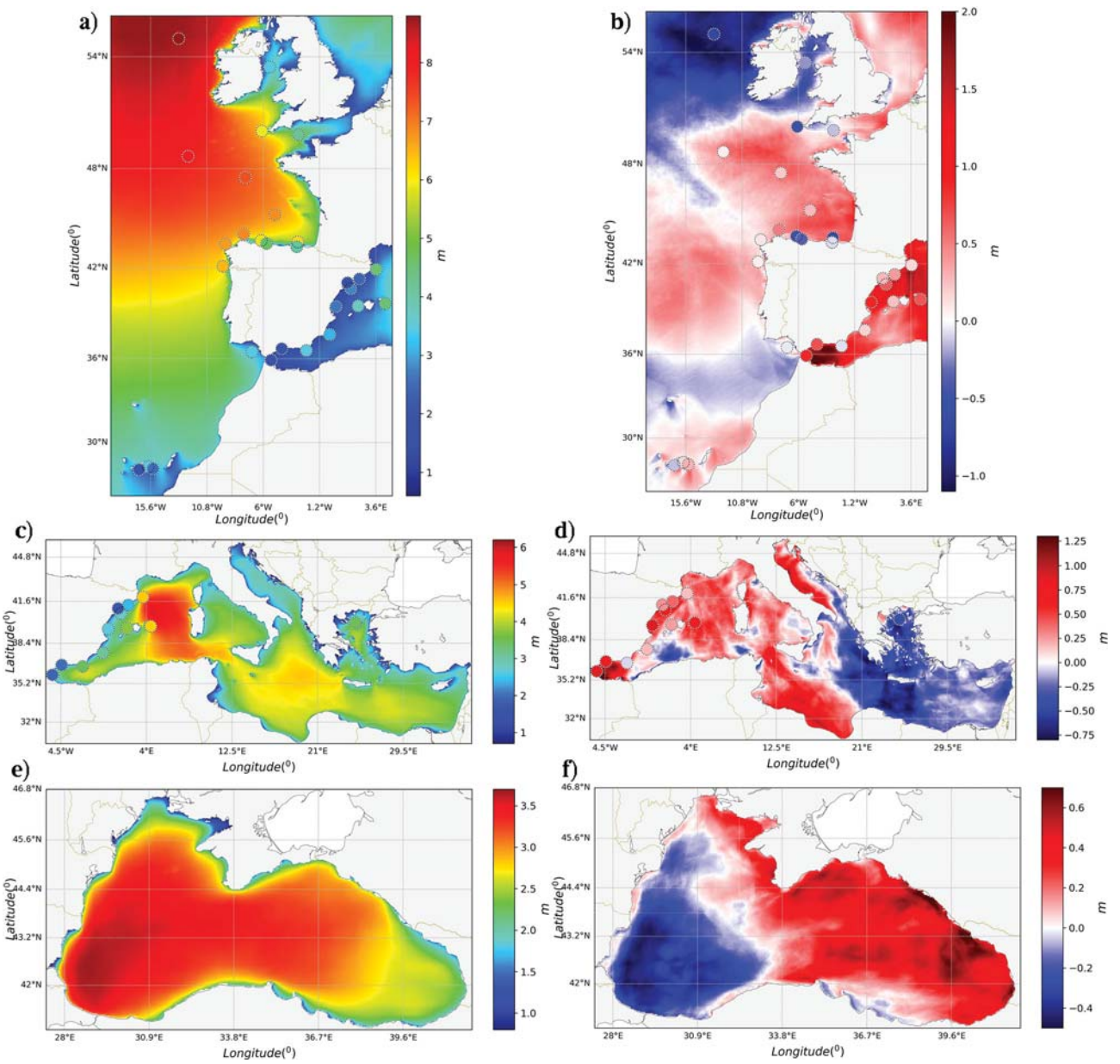

Figure 2.7.1. Map of mean 99th percentile significant wave height computed from reanalysis model data and *in situ* measurements (inset circles) for the Iberian-Biscay-Ireland region (a) (product ref. 2.7.22 and 2.7.1), Mediterranean Sea (c) (product ref. 2.7.16 and 2.7.3) and Black sea (e) (product ref. 2.7.14). Map of 99th percentile anomaly in 2017 for the Iberian-Biscay-Ireland region (b) (product ref. 2.7.11 and 2.7.5), Mediterranean Sea (b) (product ref. 2.7.24 and 2.7.7) and Black sea (f) (product ref. 2.7.13).

each year of data, from 1993 to 2016 for sea level, and from 2000 to 2016 for waves and sea surface temperature. Once the datasets based on models and observations are obtained, results from buoys and tide gauges are superimposed on the percentile maps generated from the model multi-year products (Figures 2.7.1–2.7.3 – left panels). In a second step, this process is repeated for the data of year 2017. Finally, 2017 and mean data are subtracted, producing, for each variable, a 2017 anomaly map (Figures 2.7.1–2.7.3 – right panels). For in-situ data, a minimum number of years (15 for tide gauges and 10 for buoys) with a percentage of valid measurements larger than 70% is required for a station to be included in the study. To avoid problems related to changes in reference level, all sea level data was detrended by subtracting each year the annual mean. This does not affect the main objective of the study, to analyse how anomalous 2017 was in terms of extremes.

For several regions the lack of data at CMEMS made impossible the analysis of some variables, as shown in the following sections.

2.7.1. Extremes variability in the Iberian-Biscay-Ireland area.

Waves

Figure 2.7.1(a) shows that wave extremes vary with latitude (Pontes 1998), being larger in northern seas (99th percentile larger than 8 m). The buoys in the area show results consistent with the model. Some exceptions are present, corresponding to some stations that are moored in shallow water (i.e. Gijón coastal buoy to the north of Spain), were local effects are not resolved by the model.

The year 2017 shows positive anomalies in most of the domain (Figure 2.7.1(b)), with values up to 1 m. In contrast, the anomalies are negative west of Ireland (−1 m) and around 34°N. The map of 2017 anomalies, presenting bands of positive and negative values depending on latitude, is consistent with the well-known yearly North–South displacement of the storm tracks. These latitudinal displacements alter the wind patterns over the region and, therefore, the extreme waves.

In general, there is good agreement between the 2017 data from model (product ref. 2.7.11) and from observations (product ref. 2.7.5), but with some exceptions. Off the North coast of Spain, some buoys show negative anomalies in a region where the model shows positive values. This is most likely linked to extreme values not captured by the buoys due to malfunction during severe individual storm events.

Sea Surface Temperature

Sea surface temperature mean 99th percentile in the Iberian-Biscay-Ireland area (Figure 2.7.2(a)) is strongly dependent on latitude, with higher values towards the South (Locarnini et al. 2013). Also visible is the upwelling signal off the African and western Iberian Peninsula coasts, present because the maximum extreme values

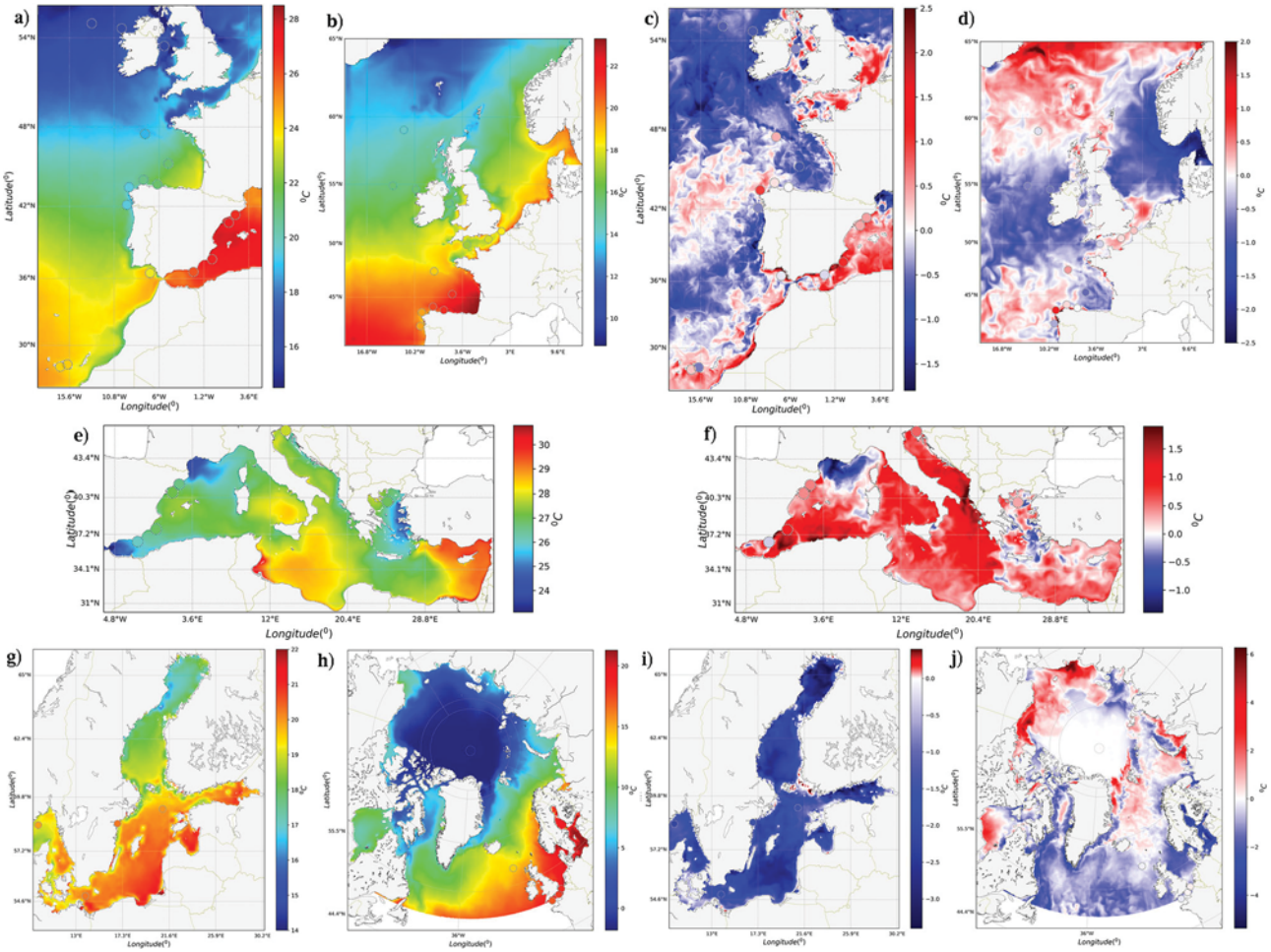

Figure 2.7.2. Map of mean 99th percentile sea surface temperature computed from reanalysis model data and *in situ* measurements (inset circles) for the Iberian-Biscay-Ireland region (a) (product ref. 2.7.10 and 2.7.1), North-West Shelf region (b) (product ref. 2.7.18 and 2.7.2), Mediterranean Sea (e) (product ref. 2.7.15 and 2.7.3), Baltic Sea (g) (product ref. 2.7.20 and 2.7.4) and Arctic Ocean (h) (product ref. 2.7.26). Map of 99th percentile anomaly in 2017 for the Iberian-Biscay-Ireland region (c) (product ref. 2.7.12 and 2.7.5), North-West Shelf region (d) (product ref. 2.7.17 and 2.7.6), Mediterranean Sea (f) (product ref. 2.7.23 and 2.7.7), Baltic Sea (g) (product ref. 2.7.19 and 2.7.8) and Arctic Ocean (h) (product ref. 2.7.25).

occur in summer, coinciding with upwelling events (Ambar and Días 2008)

The level of consistency with in-situ measurements (product ref. 2.7.1) is excellent. This agreement is due to the accuracy of the modelled product and because sea surface temperature extremes occur in the summer, when malfunctions on the buoys are rare due to mild weather conditions, and therefore high values are usually properly captured.

Results for 2017 (Figure 2.7.2(c)) show negative anomalies in most of the Atlantic domain, with values around −1°C, except in a band centred at 42°N and in the south, around the Canary Islands, where positive values can be found (~1°C). The African coast shows a positive anomaly of the extremes, reflecting a weaker than usual upwelling during the extreme temperature events at the region. Positive anomalies can also be seen in the English Channel. Buoy and model results for 2017 extremes are in good agreement.

Sea Level

Spatial differences in the mean 99th percentile of sea level reflect mainly the large differences in tidal amplitude in the region (Figure 2.7.3(a)): highest sea levels are found in the waters surrounding the British Isles and in the English Channel, where the astronomical tide is amplified (Pugh 2004). The mean 99th percentile of sea level is in considerable agreement for both model and *in situ* data at most of the stations.

Figure 2.7.3(b) shows positive anomalies (<0.1 m) for year 2017 below 40°N in the Atlantic, and negative values northwards. These anomalies agree well for both model and tide gauge data along the Spanish coast (very small and even negative anomalies in year 2017) and in the Mediterranean part of the Iberian-Biscay-Ireland domain, where sea level variability is lower (tide amplitude <0.5 m). Largest positive and negative anomalies for year 2017 (−0.3 to 0.5 m) are present around the British Isles and the English Channel.

In the Western coast of the British Isles the mean percentiles from the model are in generally good agreement with tide gauge data. This is clear in higher resolution plots (not shown). However, the anomalies for year 2017 reveal differences between tide gauge data (very small or zero values) and model data (larger positive and negative values). Differences in this overlapping region between this model and the one used for the North-West Shelf analysis (product ref. 2.7.17 and 2.7.18) are also evident. This is due to different astronomical tide propagation in the two different configurations of the Iberian-Biscay-Ireland model for the period 1993–2016 (product ref. 2.7.10) and for year 2017 (product ref. 2.7.12): both models have different spatial resolutions (1/12° vs. 1/36° respectively) and this is important for modelling the astronomical tide in coastal regions with complex bathymetry and orography (Shum et al. 1997; Turner et al. 2013).

2.7.2. Extremes variability in North-West Shelf region

Sea Surface Temperature

The mean results (Figure 2.7.2(b)) show the latitudinal dependence of 99th percentile sea surface temperature, with values ranging from 22°C at 40°N to 9°C near Iceland. The shallower waters of the North Sea present warmer extreme values than those at equivalent latitudes in the Atlantic.

2017 (Figure 2.7.2(d)) show positive anomalies in north and south of the domain. There is an extensive area of positive anomaly in the north-east region, extending to the coast of Iceland. This warm anomaly extends onto the North-West Shelf around north-eastern Scotland and is possibly advected with the Fair Isle current into the North Sea. This is also visible around north-eastern Scotland, from Aberdeen to north of the Orkneys, and near the Hebrides. There is a positive anomaly extending from the English Channel into the Southern Bight of the southern North Sea, which is coincident in both the North-West Shelf and Iberian-Biscay-Ireland model domains. There is a narrow band of positive anomaly along the coast of the northern part of the Bay of Biscay, near Nantes, although the exact extent varies between the North-West Shelf and Iberian-Biscay-Ireland domains. Anomaly values are negative in the rest of the domain, especially near the Baltic Sea and south of the Scandinavian Peninsula.

In general, model and in-situ results are very consistent.

Sea Level

The annual mean of the 99th percentile sea level map (product ref. 2.7.18) for the North-West Shelf reflects the spatial distribution of tidal ranges (Figure 2.7.3(c)), consistent with the M_2 amplitude co-tidal chart (O'Dea et al. 2012, 2017). Mean 99th percentiles model reanalysis data (product ref. 2.7.18) are consistent (Figure 2.7.3 (c)) with the tide gauge data (product ref. 2.7.2).

The 2017 99th percentile value is very similar to that of the reanalysis period over most of the domain, in both pattern and amplitude (not shown) and this is reflected by the anomaly map (Figure 2.7.3(d)) which has values ranging from −10 cm to +40 cm. The largest differences occur in the North Sea, with 2017 being up to 30 cm higher in 2017, than in the mean. This is particularly significant when looking at the percentage differences (not shown) as the mean tidal ranges are relatively low here (see Figure 2.7.3(c)) – 2017 was >60% higher than in

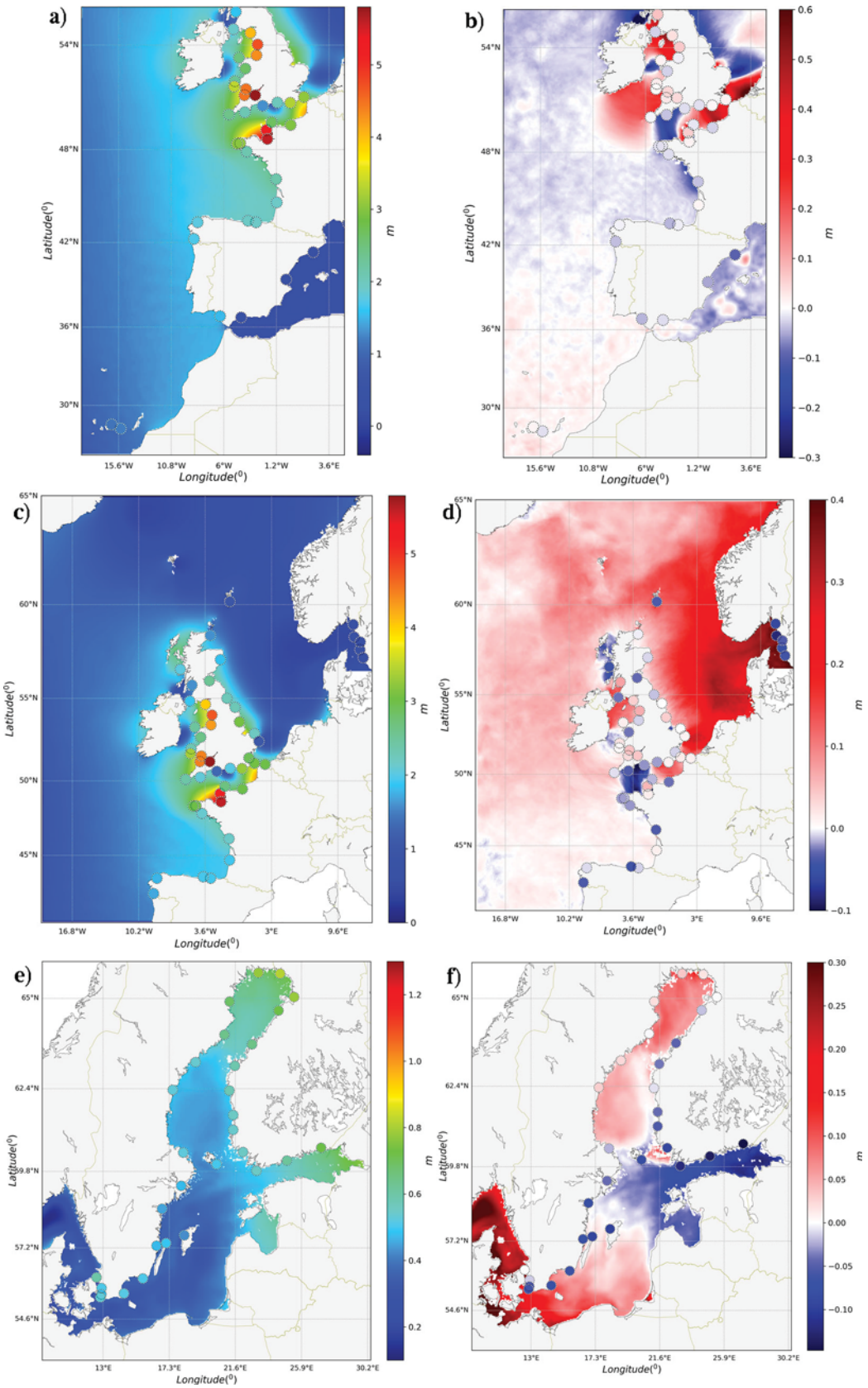

Figure 2.7.3. Map of mean 99th percentile sea level computed from reanalysis model data and *in situ* measurements (inset circles) for the Iberian-Biscay-Ireland region (a) (product ref. 2.7.10 and 2.7.1), North-West Shelf region (c) (product ref. 2.7.18 and 2.7.2) and Baltic Sea (e) (product ref. 2.7.20 and 2.7.4). Map of 99th percentile anomaly in 2017 for the Iberian-Biscay-Ireland region (b) (product ref. 2.7.12, 2.7.5 and 2.7.9), North-West Shelf region (d) (product ref. 2.7.17, 2.7.6 and 2.7.9) and Baltic Sea (f) (product ref. 2.7.19 and 2.7.8).

the reanalysis period. This appears to be a large difference in the western English Channel, with the 2017 extreme sea levels being less than in the reanalysis period, by ~10 cm, but given the large tidal range here, is ~10% lower.

Interestingly, in the Skagerrak and Kattegat there is a disagreement between the model and *in situ* anomalies (up to 40 cm difference), with the tide gauges showing a negative anomaly, while the model shows a positive bias. This is likely a result of the Baltic boundary conditions used in the North-West Shelf reanalysis. There is a relatively good agreement between the model and tide gauges anomalies around the UK.

North-West Shelf and Iberian-Biscay-Ireland model generally a good spatial agreement. Both show the negative anomaly in the eastern English Channel, and across the centre of the Irish Sea, with adjacent positive anomaly in the western English Channel and Celtic Sea, and Irish Sea. To the west of the UK there is a large difference in the sea level anomaly, with the Iberian-Biscay-Ireland showing a negative anomaly in the central and northern North Sea. This difference could be related, as previously discussed, to the different Iberian-Biscay-Ireland tidal solutions in reanalysis and operational products.

2.7.3. Extremes variability in the Mediterranean region

Waves

Figure 2.7.1(c) shows that the highest values of the mean annual 99th percentile are located where high winds and long fetch are simultaneously present. Specifically, such values extend from the Gulf of Lion to southwestern Sardinia through the Balearic Sea. They result from northerly winds dominant in the western Mediterranean Sea (Mistral or Tramontana), that are accelerated by orography (Menendez et al. 2014) and act over a large area. In the Ionian Sea, the northerly Mistral wind is still the main cause of high waves whilst in the Aegean and Levantine Seas, high waves are caused by the northerly Bora winds, prevalent in winter, and the northerly Etesian winds, prevalent in summer (Lionello et al. 2006; Chronis et al. 2011; Menendez et al. 2014).

During the year 2017 (Figure 2.7.1(d)), the positive anomalies in the west (up to 1.25 m) and central-west Mediterranean and the negative anomalies in the east (up to −0.75 m) are in turn indicative of stronger than usual winds in the former case and weaker than usual in the latter. Model data and in-situ data show consistent results.

Sea Surface Temperature

The mean annual 99th percentile (Figure 2.7.2(e)) in the period 1993–2016 presents lower values in the Alborán Sea, linked to the inflow of cold Atlantic waters through the Gibraltar Strait, in the Gulf of Lion, caused by the strong Mistral wind, and in the North Aegean Sea, which also can be explained by the action of local winds; while highest sea surface temperature values are mainly located in the Levantine Sea, which is the warmest area of the Mediterranean Sea, and in the Gulf of Gabes.

Results for the year 2017 (Figure 2.7.2(f)) are characterised by very large positive anomalies in most of the domain, with maximum value of around 1.8°C. Negative anomalies are located in limited areas (Gulf of Lion and Eastern Aegean Sea) with values down to −1.5°C.

2.7.4. Extremes variability in the Baltic region

Waves

The distribution of extreme significant wave heights during 2017 from product reference 2.7.21 corresponds to the fetch limited wind waves generated by prevailing westerly and south-westerly winds (Isemer et al. 2008). The highest significant wave heights up to 4.5 m were in the southeastern Baltic Proper remaining over 4 m until the entrance of the Gulf of Finland. In the Gulf of Finland wave growth is limited by the narrowness of the gulf (Tuomi et al. 2011) and therefore percentiles remain in range of 2–3 m. In the northern Baltic extreme significant wave heights reach up to 4 and 3.5 m in Bothnian Sea and Bothnian Bay respectively.

It is worth to mention, nevertheless, that results from the wave field for the year 2017 (not shown) are in good agreement with the data from the two buoys available at the region.

There is no multi-year CMEMS wave product available for the Baltic at this moment. Therefore the 2017 anomaly values can't be computed. However, the differences were evaluated using published results of extreme wave heights from long-term wave field simulations (Björkqvist et al. 2017). The wave conditions in the Bothnian Bay were more severe in 2017 exceeding long-term percentiles by approximately 0.50 m. In the rest of the Baltic the 2017 significant wave height extremes remained within the range of ±0.25 m to the reported long-term percentiles by Björkqvist et al. (2017). In the calculation of wave statistics for 99th percentiles Björkqvist et al. (2017) excluded wave data from the calculations during ice covered period, while in CMEMS zero significant wave height values were used.

Sea Surface Temperature

Mean sea surface temperature extremes (product reference 2.7.20) show latitudinal gradient with temperatures in range of 20–22°C in the southern and 17–19°C in the northern part (Figure 2.7.2(g)). Lower sea surface

temperature values along the western coast of the Baltic Sea represent the most frequent upwelling areas (Myrberg and Andrejev 2003; Lehmann et al. 2008, 2012) in response to the prevailing winds from the southwest (Isemer et al. 2008). In the Gulf of Finland, low temperature is obvious along both the northern and the southern coasts. These low value regions are due to coastal upwelling during different periods. The upwelling area along the northern coast is more extensive than along the southern coast, but the sea surface temperature values are slightly higher. The western part of the southern coast of the Gulf of Finland is described with lower sea surface temperature and wider offshore extent of the upwelling zone. The upwelling in the area is caused by strong wind events from the northeast. This peculiarity arises from shallower thermocline position and steeper slope on the southern coast of the Gulf of Finland (Kikas and Lips 2016). The eastern part of the southern Gulf of Finland is less affected by the upwellings, as there the sea surface temperature does not distinguish from the open sea area. Only long-lasting winds from the east or sequence of the storm from the east can cause intensive upwelling and drop of the sea surface temperature there (Suursaar and Aps 2007; Väli et al. 2011).

2017 presents a very clear negative anomaly over the whole domain (Figure 2.7.2(i)), both at the measuring stations (product ref. 2.7.8) and in the model data (product ref. 2.7.19). Sea surface temperature extremes show differences of −2 to −3°C from the mean. There are clear signals of upwelling events along the northern and eastern coasts of the Baltic Proper as well as on the northern coast of the Gulf of Finland. This corresponds to typical upwelling pattern with prevailing south-westerly winds. Especially distinctive is the upwelling zone extending along the northern coast of the Gulf of Finland, which is clearly visible on maps of sea surface temperature extremes for 2017 (not shown). There was no major upwellings on the southern coast of the Gulf of Finland, therefore the anomaly shows higher temperatures there compared to offshore/background differences.

Sea Level

Mean sea level 99th percentiles range from approximately 0.4–0.8 m (Figure 2.7.3(e)) in the Baltic (product reference 2.7.20). The extremes in the Baltic Sea are mainly caused by wind setup amplified by the seiches and remotely generated long waves (Hünicke et al. 2015). The extremes are underestimated by about 0.1 m in the model. The discrepancy increases towards the southern Baltic Sea, being largest in the Danish Sounds. This could be attributed to the possible mismatch between model and measurements in the transition zone between the North Sea and the Baltic Sea. The sea level extremes are slightly lower in the open part of the sea compared to the coastal areas, affected by the wind setup.

The anomaly of the sea level extremes in 2017 (Figure 2.7.3(f)) is in the range of ±0.15 m and −0.15–0.05 m in the model (product reference 2.7.19) and in the measurements (product ref. 2.7.8), respectively, which are not significant differences from the long-term mean extremes. Within this small range of variation, the model and measurements tend to agree in the Gulf of Bothnia and in the Gulf of Finland. The most notable differences are for the southern part of the Baltic Proper, where model results/measurements show higher/lower sea level extremes than the long-term mean. At the local scale, the model shows high sea level around the Archipelago Sea, but the measurements have lower extremes there. Obviously, local positive sea level anomalies there are a model artefact, as measurements show continuous increase in sea level anomaly from the Gulf of Finland through the Archipelago Sea to the Bothnian Sea.

2.7.5. Extremes variability in the Black Sea region

Waves

Since there are no available wave observations in this region matching the requirements of this study, the analysis for this domain is based on model data only. Figure 2.7.1(e) shows a well-known pattern demonstrating that the highest values of the mean annual 99th percentile are in the areas where high winds and long fetch are simultaneously present (from multi-year wave product ref. 2.7.14). The mean extreme values in the region tend to be largest in the western Black Sea, with values as high as 3.5 m. Values in the eastern part of the basin are around 2.5 m (Behrens et al. 2019).

In 2017 (product reference 2.7.13), the highest values of the 99th percentile are in the central part of the basin (between 34 and 36 deg. E, not shown). In consequence, the anomaly values for 2017 show a strong longitudinal dependency, with negative anomalies in the western part of the Black Sea (up to 0.5 m) and positive ones in the central and eastern Black Sea (up to 0.7 m, Figure 2.7.1(f)). Results from wave fields for 2017 are in good agreement with satellite data (Jason-3 and Sentinel-3a) as well as with the Varna wave-buoy, showing values of mean SWH up to 1.8 m in the centre of the Black Sea. (Quality Information Document of 2.7.13 product).

2.7.6. Extremes variability in the Arctic region

Sea Surface Temperature

The distribution of the mean annual 99th percentile of sea surface temperature (Figure 2.7.2(h)) reflects the

dominant currents of the region. The warmest waters with the subarctic (10–20°C) occur within the region of the northern European continental shelf and the North Atlantic Current, as well as within its extension through the Nordic Seas (Wekerle et al. 2017) and into the Barents Sea (Skagseth 2008). Relatively warmer (5–10° C) waters also extend northward to the west of Svalbard (Seidov et al. 2015) carried by the western branch of the Norwegian Atlantic Current. The Bering Strait connects the Arctic to the Pacific and exhibits relatively warm surface waters (>5°C) which extend into the Chukchi Sea (Seidov et al. 2015). Cold Polar Surface Water (Rudels 2015) which exists throughout the Arctic basin extends southwards through the Canadian Arctic Archipelago and along the east coast of Greenland, due to presence of the Greenland boundary current.

Anomalies of SST within the Arctic region and its extended domain during 2017 show a complex regional pattern of positive and negative anomalies. Negative anomalies are found throughout the northern Atlantic and much of the Canadian archipelago and the Laptev Sea. Positive anomalies of up to 6°C are found in the East Siberian Sea, the Beaufort Sea and the coastal regions of the Kara Sea. Positive anomalies of up to 3° C are seen throughout the Greenland Sea and in the northern Barents Sea. Positive anomalies of up to 4°C occur in the Chukchi Sea and in Hudson Bay.

References

Section 2.1. Sea surface winds and Ekman pumping

Bakun A, Black BA, Bograd SJ, Garcia Reyes M, Miller AJ, Rykaczewski RR, Sydeman WJ. 2015. Anticipated effects of climate change on coastal upwelling ecosystems. Curr Clim Change Rep. 1:85. doi:10.1007/s40641-015-0008-4.

Belmonte Rivas M, Stoffelen A. 2019. Characterizing ERA-Interim and ERA5 surface wind biases using ASCAT. Ocean Sci. 15:831–852. doi:10.5194/os-15-831-2019.

Bograd SJ, Lynn RJ. 2001. Physical-biological coupling in the California current during the 1997–99 El Niño-La Niña cycle. Geophys Res Lett. 28(2):275–278. doi:10.1029/2000GL012047.

Chen G, Han W, Li Y, Wang D. 2016. Interannual variability of equatorial eastern Indian ocean upwelling: local versus remote forcing. J Phys Oceanogr. 46:789–807. doi:10.1175/JPO-D-15-0117.1.

de Kloe J, Stoffelen A, Verhoef A. 2017. Improved use of scatterometer measurements by using stress-equivalent reference winds. IEEE J Sel Topics Appl Earth Observ In Remote Sens. 10(5). doi:10.1109/JSTARS.2017.2685242.

Ekman VW. 1905. On the influence of the Earth's rotation on ocean-currents. Arkiv for Matematik, Astronomi och Fysik. 2(11):1–52.

Hall A, Visbeck M. 2002. Synchronous variability in the southern hemisphere atmosphere, sea ice, and ocean resulting from the annular mode. J Clim. 15:3043–3057. doi:10.1175/1520-0442(2002)015<3043:SVITSH>2.0.CO;2.

Holland PR, Kwok R. 2012. Wind-driven trends in Antarctic sea-ice drift. Nature Geosc. 5:872–875. doi:10.1038/ngeo1627.

Large WG, McWilliams JC, Doney SC. 1994. Oceanic vertical mixing: a review and a model with a nonlocal boundary layer parameterization. Rev Geophys. 32(4):363–403. doi:10.1029/94RG01872.

Lorenz EN. 1955. Available potential energy and the maintenance of the general circulation. Tellus. 7:157–167. doi:10.1111/j.2153-3490.1955.tb011148.x.

Pelegri JL, Marrero-Diaz A, Ratsimandresey AW. 2006. Nutrient irrigation in the North Atlantic. Prog in Oceanogr. 70:366–406. doi:10.1016/j.pocean.2006.03.018.

Raphael MN, Marshall GJ, Turner J, Fogt RL, Schneider D, Dixon DA, Hosking JS, Jones JM, Hobbs WR. 2016. The Amundsen sea low: variability, change, and impact on Antarctic climate. Bull Am Meteorol Soc. 97:111–121. doi:10.1175/BAMS-D-14-00018.1.

Risien CM, Chelton DB. 2008. A global climatology of surface wind and wind stress fields from eight years of Quikscat scatterometer data. J Phys Oceanogr. 38:2379–2413. doi:10.1175/2008JPO3881.1.

Spall MA, Pickart RS. 2003. Wind-driven recirculations and exchange in the Labrador and Irminger Seas. J Phys Oceanogr. 33:1829–1845. doi:10.1175/2384.1.

Thompson DWJ, Solomon S. 2002. Interpretation of recent Southern Hemisphere climate change. Science. 296:895–899. doi:10.1126/science.1069270.

Turner J, Phillips T, Hosking JS, Marshall GJ, Orr A. 2013. The Amundsen sea low. Int J Clim. 33(7):1818–1829. doi:10.1002/joc.3558.

Section 2.2. The seasonal intensification of the slope Iberian Poleward Current

Charria G, Lazure P, Le Cann B, Serpette A, Reverdin G, Louazel S, Batifoulier F, Dumas F, Pichon A, Morel Y. 2013. Surface layer circulation derived from Lagrangian drifters in the Bay of Biscay. J Mar Syst. 109–110:S60–S76.

Declerck A, Delpey M, Rubio A, Ferrer L, Basurko OC, Mader J, Louzao M. 2019. Transport of floating marine litter in the coastal area of the south-eastern Bay of Biscay: A Lagrangian approach using modelling and observations. J Oper Oceanogr. doi:10.1080/1755876X.2019.1611708.

González M, Uriarte A, Fontán A, Mader J, Gyssels P. 2004. Marine dynamics. In: Borja A, Collins M, editors. Oceanography and marine environment of the Basque Country. Vol. 70, Elsevier Oceanography Series. Amsterdam: Elsevier; p. 133–157.

Herbert G, Ayoub N, Marsaleix P, Lyard F. 2011. Signature of the coastal circulation variability in altimetric data in the southern Bay of Biscay during winter and fall 2004. J Mar Syst. 88(2):139–158. doi:10.1016/j.jmarsys.2011.03.004.

Kaplan DM, Lekien F. 2007. Spatial interpolation and filtering of surface current data based on open-boundary modal analysis. J Geophys Res Oceans. 112:C12007. doi:10.1029/2006JC003984.

Lazure P. 1997. La circulation des eaux dans le Golfe de Gascogne. In: 10émes rencontres interregionales de l'AGLIA. Saint Jean de Luz; p. 83–88.

Le Cann B, Serpette A. 2009. Intense warm and saline upper ocean inflow in the southern Bay of Biscay in autumn-winter 2006–2007. Cont Shelf Res. 29(8):1014–1025.
Pingree RD, Le Cann B. 1992. Three anticyclonic Slope Water Oceanic eDDIES (SWODDIES) in the southern Bay of Biscay in 1990. Deep-Sea Res. 39(7/8):1147–1175.
Rubio A, Caballero A, Orfila A, Hernández-Carrasco I, Ferrer L, González M, Solabarrieta L, Mader J. 2018. Eddy-induced cross-shelf export of high Chl-a coastal waters in the SE Bay of Biscay. Remote Sens Environ. 205. doi:10.1016/j.rse.2017.10.037.
Rubio A, Fontán A, Lazure P, González M, Valencia V, Ferrer L, Mader J, Hernández C. 2013. Seasonal to tidal variability of currents and temperature in waters of the continental slope, SE Bay of Biscay. J Mar Syst. 109–110:S121–S133.
Rubio A, Reverdin G, Fontán A, González M, Mader J. 2011. Mapping near-inertial variability in the SE Bay of Biscay from HF radar data and two offshore moored buoys. Geophys Res Lett. 38(19):L19607.
Solabarrieta L, Frolov S, Cook M, Paduan J, Rubio A, González M, Mader J, Charria G. 2016. Skill assessment of HF radar-derived products for Lagrangian simulations in the Bay of Biscay. J Atmos Ocean Technol. 33:2585–2597. doi:10.1175/JTECH-D-16-0045.1.
Solabarrieta L, Rubio A, Cárdenas M, Castanedo S, Esnaola G, Méndez FJ, Medina R, Ferrer L. 2015. Probabilistic relationships between wind and Surface water circulation patterns in the SE Bay of Biscay. Ocean Dyn. 65(9):1289–1303.
Solabarrieta L, Rubio A, Castanedo S, Medina R, Fontán A, González M, Fernández V, Charria G, Hernández C. 2014. Surface water circulation patterns in the southeastern Bay of Biscay: new evidences from HF radar data. Cont Shelf Res. 74:60–76.
Teles-Machado A, Peliz A, McWilliams J, Dubert J, Le Cann B. 2016. Circulation on the northwestern Iberian margin: swoddies. Prog Oceanogr. 140:116–133. doi:10.1016/j.pocean.2015.09.011.

Section 2.3. Mediterranean deep and intermediate water mass properties

Ben Ismail S, Schroeder K, Sammari C, Gasparini GP, Aleya L. 2014. Interannual variability of water mass properties in the Tunisia–Sicily channel. J Mar Sys. 135:14–28.
Bethoux JP, Gentili B. 1999. Functioning of the Mediterranean Sea: past and present changes related to fresh water input and climatic changes. J Mar Syst. 20:33–47.
Cook BI, Anchukaitis KJ, Touchan R, Meko DM, Cook ER. 2016. Spatiotemporal drought variability in the Mediterranean over the last 900 years. J Geophys Res Atmos. 121:2060–2074.
Gačić M, Schroeder K, Civitarese G, Cosoli S, Vetrano A, Eusebi Borzelli GL. 2013. Salinity in the Sicily channel corroborates the role of the Adriatic–Ionian Bimodal Oscillating System (BiOS) in shaping the decadal variability of the Mediterranean overturning circulation. Ocean Sci. 9:83–90.
Gasparini GP, Ortona A, Budillon G, Astraldi M, Sansone E. 2005. The effect of the eastern Mediterranean transient on the hydrographic characteristics in the Strait of Sicily and in the Tyrrhenian Sea. Deep-Sea Res. 52:915–935.
Giorgi F. 2006. Climate change Hot-spots. Geophys Res Lett. 33:L08707.
Josey SA, Somot S, Tsimplis M. 2011. Impacts of atmospheric modes of variability on Mediterranean Sea surface heat exchange. J Geophys Res. 116:C02032.
Naranjo C, García-Lafuente J, Sammartino S, Sánchez-Garrido JC, Sánchez-Leal R, Jesús Bellanco M. 2017. Recent changes (2004–2016) of temperature and salinity in the Mediterranean outflow. Geophys Res Lett. 44:5665–5672.
Rixen M, Beckers JM, Levitus S, Antonov J, Boyer T, Maillard C, Fichaut M, Balopoulos E, Iona S, Dooley H, et al. 2005. The western Mediterranean deep water: a proxy for climate change. Geophys Res Lett. 32:L12608.
von Schuckmann K, Le Traon P, Alvarez-Fanjul E, Axell L, Balmaseda M, Breivik L-A, Brewin RJW, Bricaud C, Drevillon M, Drillet Y, et al. 2018. The Copernicus marine service ocean state report issue 2. J Oper Oceanogr. 11 (sup1): s1–S142. doi:10.1080/1755876X.2018.14892808.
Schroeder K, Chiggiato J, Bryden HL, Borghini M, Ben Ismail S. 2016. Abrupt climate shift in the western Mediterranean Sea. Sci Rep. 6:23009.
Schroeder K, Chiggiato J, Josey SA, Borghini M, Aracri S, Sparnocchia S. 2017. Rapid response to climate change in a marginal sea. Sci Rep. 7:4065.
Schroeder K, Millot C, Bengara L, Ben Ismail S, Bensi M, Borghini M, Budillon G, Cardin V, Coppola L, Curtil C, et al. 2013. Long-term monitoring programme of the hydrological variability in the Mediterranean Sea: a first overview of the hydrochanges network. Ocean Sci. 9:1–24.
Vargas-Yáñez M, García-Martínez MC, Moya F, Balbín R, López-Jurado JL, Serra M, Zunino P, Pascual J, Salat J. 2017. Updating temperature and salinity mean values and trends in the western Mediterranean: THE RADMED project. Progr Ocean. 157:27–46.

Section 2.4. Phytoplankton blooms in the Baltic Sea

Brewin RJW, Sathyendranath S, Müller D, Brockmann C, Deschamps P-Y, Devred E, Doerffer R, Fomferra N, Franz B, Grant M, et al. 2015. The ocean colour climate change initiative: III. A round-robin comparison on in-water bio-optical algorithms. Remote Sens Environ. 162:271–294. doi:10.1016/j.rse.2013.09.016.
Fennel K. 1999. Convection and the timing of phytoplankton spring blooms in the western Baltic Sea. Estuar Coast Shelf Sci. 49(1):113–128. doi:10.1006/ecss.1999.0487.
Groetsch PMM, Simis SGH, Eleveld MA, Peters SWM. 2016. Spring blooms in the Baltic Sea have weakened but lengthened from 2000 to 2014. Biogeosciences. 13(17):4959–4973. doi:10.5194/bg-13-4959-2016.
Hansson M, Håkansson B. 2007. The Baltic algae watch system – a remote sensing application for monitoring cyanobacterial blooms in the Baltic Sea. J Appl Remote Sens. 1. doi:10.1117/1.2834769.
Hansson M, Pamberton P, Håkansson B, Reinart A, Alikas K. 2010. Operational nowcasting of algal blooms in the Baltic Sea using MERIS and MODIS. ESA Living Planet Symposium; Bergen, Norway. Vol. 686.
HELCOM. 2015. HELCOM eutrophication assessment manual. [accessed 2018 Jul 22]. http://www.helcom.fi/Documents/Eutrophication assessment manual.pdf.
Kahru M, Elmgren R, Di Lorenzo E, Savchuk O. 2018. Unexplained interannual oscillations of cyanobacterial

blooms in the Baltic Sea. Sci Rep. 8(1):6365. doi:10.1038/s41598-018-24829-7.
Kahru M, Nõmmann S. 1990. The phytoplankton spring bloom in the Baltic Sea in 1985, 1986: multitude of spatio-temporal scales. Cont Shelf Res. 10(4):329–354. doi:10.1016/0278-4343(90)90055-Q.
Mélin F, Vantrepotte V, Chuprin A, Grant M, Jackson T, Sathyendranath S. 2017. Assessing the fitness-for-purpose of satellite multi-mission ocean color climate data records: a protocol applied to OC-CCI chlorophyll-a data. Remote Sens Environ. 203:139–151. doi:10.1016/j.rse.2017.03.039.
O'Reilly JE, Maritorena S, Mitchell BG, Siegel DA, Carder KL, Garver SA, Kahru M, McClain C. 1998. Ocean color chlorophyll algorithms for SeaWiFS. J Geophys Res Ocean. 103 (C11):24937–24953. doi:10.1029/98JC02160.
Pitarch J, Volpe G, Colella S, Krasemann H, Santoleri R. 2016. Remote sensing of chlorophyll in the Baltic Sea at basin scale from 1997 to 2012 using merged multi-sensor data. Ocean Sci. 12(2):379–389. doi:10.5194/os-12-379-2016.
Raudsepp U, She J, Brando VE, Kõuts M, Lagemaa P, Sammartino M, Santoleri R. 2018. Baltic inflows. In: von Schuckmann K, Le Traon P-Y, Smith N, Pascual A, Brasseur P, Fennel K, Djavidnia S, editors. Copernicus marine service ocean state report, issue 2. J Oper Oceanogr. 11 (sup1):s13–s16. doi:10.1080/1755876X.2018.1489208.
Sathyendranath S, Brewin RJW, Jackson T, Mélin F, Platt T. 2017. Ocean-colour products for climate-change studies: what are their ideal characteristics? Remote Sens Environ. 203:125–138. doi:10.1016/j.rse.2017.04.017.
Siegel DA. 2002. The north Atlantic spring phytoplankton bloom and Sverdrup's critical depth hypothesis. Science. 296(5568):730–733. doi:10.1126/science.1069174.
Wan Z, Bi H, She J. 2013. Comparison of two light attenuation parameterization focusing on timing of spring bloom and primary production in the Baltic Sea. Ecol Modell. 259:40–49. doi:10.1016/j.ecolmodel.2013.03.010.
Wasmund N, Dutz J, Pollehne F, Siegel H, Zettler ML. 2017. Biological assessment of the Baltic Sea 2016. Warnemünde: Leibniz Institute for Baltic Sea Research. Mar Sci Rep. 105. doi:10.12754/msr-2017-0105.
Wasmund N, Dutz J, Pollehne F, Siegel H, Zettler ML. 2018. Biological assessment of the Baltic Sea 2017. Warnemünde: Leibniz Institute for Baltic Sea Research. Mar Sci Rep. 108. doi:10.12754/msr-2018-0108.

Section 2.5. Cod reproductive volume potential in the Baltic Sea

Cardinale M, Arrhenius F. 2000. The influence of stock structure and environmental conditions on the recruitment process of Baltic cod estimated using a generalized additive model. Can J Fish Aquat Sci. 57(12):2402–2409. doi:10.1139/f00-221.
Cardinale M, Modin J. 1999. Changes in size-at-maturity of Baltic cod (*Gadus morhua*) during a period of large variations in stock size and environmental conditions. Fish Res. 41(3):285–295. doi:10.1016/S0165-7836(99)00021-1.
EFSA Publication, Nielsen R. 1998. Mechanisms influencing long term trends in reproductive success and recruitment of Baltic cod: implication for fisheries management: CORE program final report. EU Commission DGXIV, I–III. [s.l.]: European Commission. EU AIR2. CT94-1226.
Heikinheimo O. 2008. Average salinity as an index for environmental forcing on cod recruitment in the Baltic Sea. Boreal Environ Res. 13:457–464.
Hinrichsen H-H, von Dewitz B, Lehmann A, Bergström U, Hüssy K. 2017. Spatio-temporal dynamics of cod nursery areas in the Baltic Sea. Prog Oceanogr. 155:28–40. doi:10.1016/j.pocean.2017.05.007.
ICES. 2005. Report of the study group on multispecies assessment in the baltic (SGMAB); Jun 13–17; Riga, Latvia. ICES CM 2005/H:06.
ICES. 2016. Report of the Baltic fisheries assessment working group (WGBFAS); Apr 12–19; Copenhagen, Denmark. ICES HQ. ICES CM 2016/ACOM:11.
ICES. 2018. ICES advice on fishing opportunities, catch, and effort. https://doi.org/10.17895/ices.pub.4378.
Karaseva EM, Zezera AS. 2016. Causes of different impact of major Baltic inflows on cod reproduction in the Gotland basin of the Baltic Sea. Oceanology. 56(5):643–654. doi:10.1134/S0001437016040068.
Karasiova EM. 2011. Assessment of production of eggs of eastern Baltic cod (*Gadus morhua callarias* L.) on the basis of long-term ichthyoplankton data. Russ J Dev Biol. 42 (3):168–172. doi:10.1134/S1062360411030076.
Karasiova EM, Voss R, Eero M. 2008. Long-term dynamics in eastern Baltic cod spawning time: from small scale reversible changes to a recent drastic shift. ICES CM 2008/J:03.
Köster FW, Möllmann C, Hinrichsen H-H, Wieland K, Tomkiewicz J, Kraus G, Voss R, Makarchouk A, MacKenzie BR, St John MA, et al. 2005. Baltic cod recruitment – the impact of climate variability on key processes. ICES J Mar Sci. 62(7):1408–1425. doi:10.1016/j.icesjms.2005.05.004.
MacKenzie B, St John M, Wieland K. 1996. Eastern Baltic cod: perspectives from existing data on processes affecting growth and survival of eggs and larvae. Mar Ecol Prog Ser. 134:265–281. doi:10.3354/meps134265.
Plikshs M, Hinrichsen H-H, Elferts D, Sics I, Kornilovs G, Köster FW. 2015. Reproduction of Baltic cod, Gadus morhua (Actinopterygii: Gadiformes: Gadidae), in the Gotland basin: causes of annual variability. Acta Ichthyol Piscat. 45 (3):247–258. doi:10.3750/AIP2015.45.3.04.
Raudsepp U, Legeais J-F, She J, Maljutenko I, Jandt S. 2018. Baltic inflows. In: von Schuckmann K, Le Traon P-Y, Smith N, Pascual A, Brasseur P, Fennel K, Djavidnia S, editors. Copernicus marine service ocean state report, issue 2. J Oper Oceanogr. 11(sup1):s13–s16. doi:10.1080/1755876X.2018.1489208.

Section 2.6. The North Pacific Gyre Oscillation

Di Lorenzo E, Schneider N, Cobb KM, Chhak K, Franks PJS, Miller AJ, McWilliams JC, Bograd SJ, Arango H, Curchister E, et al. 2008. North Pacific gyre oscillation links ocean climate and ecosystem change. Geophysical Research Letters. 35:L08607.
Kalnay E, Kanamitsu M, Kistler R, Collins W, Deaven D, Gandin L, Iredell M, Saha S, White G, Woollen J, et al. 1996. The NCEP/NCAR 40-year reanalysis project. Bull Am Meteor Soc. 77:437–471.

Niiler P, Maximenko NA, McWilliams JC. 2003. Dynamically balanced absolute sea level of the global ocean derived from near-surface velocity observations. Geophys Res Lett. 30 (22):2164.
Walker GT, Bliss EW. 1932. World weather V. Mem R Meteorol Soc. 4:53–84.
Yi D, Gan L, Wu B, Miller AJ. 2018. The north Pacific gyre oscillation and mechanisms of its decadal variability in CMIP5 models. J Clim. 31(6):2487–2509.

Section 2.7. Sea level, sea surface temperature and SWH extreme percentiles from model results and in situ *observations in European Seas*

Ambar I, Días J. 2008. Remote sensing of coastal upwelling in the north-eastern Atlantic ocean. In: Barale V., Gade M, editors. Remote sensing of the European seas. Dordrecht: Springer. doi:10.1007/978-1-4020-6772-3_11.
Behrens A, Staneva J, Gayer G. 2019. Validation of wave model results in data sparse semi-enclosed areas like the Black Sea. J Oper Oceanogr.
Björkqvist J-V, Tuomi L, Fortelius C, Pettersson H, Tikka K, Kahma KK. 2017. Improved estimates of nearshore wave conditions in the Gulf of Finland. J Mar Syst. 71:43–53. doi:10.1016/j.jmarsys.2016.07.005.
Chronis T, Papadopoulos V, Nikolopoulos EI. 2011. QuickSCAT observations of extreme wind events over the Mediterranean and Black Seas during 2000–2008. Int J Climatol. 31:2068–2077.
Hünicke B, Zorita E, Soomere T, Madsen KS, Johansson M, Suursaar Ü. 2015. Recent change-sea level and wind waves. In: Bolle H-J, Menenti M, Rasool I, editors. Second assessment of climate change for the Baltic Sea basin. Cham: Springer; p. 155–185. doi:10.1007/978-3-319-16006-1_9.
Isemer H-J, Russak V, Tuomenvirta H. 2008. A.1.2 atmosphere. In: Bolle H-J, Menenti M, Rasool I, editors. Assessment of climate change for the Baltic Sea basin. Berlin: Springer; p. 386–392. doi:10.1007/978-3-540-72786-6.
Kikas V, Lips U. 2016. Upwelling characteristics in the Gulf of Finland (Baltic Sea) as revealed by Ferrybox measurements in 2007–2013. Ocean Sci. 12(3):843–859. doi:10.5194/os-12-843-2016.
Lehmann A, Myrberg K, Höflich K. 2012. A statistical approach to coastal upwelling in the Baltic Sea based on the analysis of satellite data for 1990–2009. Oceanologia. 54(3):369–393. doi:10.5697/oc.54-3.369.
Lehmann A, Raudsepp U, Szymelfenig M, Lips I, Matciak M, Kowalewski M, Krezel A, Burska D, Szymanek L, Ameryk A. 2008. Upwelling events, coastal offshore exchange, links to biogeochemical processes – highlights from the Baltic. Oceanologia. 50(1):95–113.
Lionello P, Rizzoli PM, Boscolo R, editors. 2006. Mediterranean climate variability. Amsterdam: Springer. (Developments in earth and environmental sciences. 4).
Locarnini RA, Mishonov AV, Antonov JI, Boyer TP, Garcia HE, Baranova OK, Zweng MM, Paver CR, Reagan JR, Johnson DR, et al. 2013. World ocean atlas 2013. In: Levitus S, Mishonov A, editors, technical editors. NOAA atlas NESDIS 73, 40 pp. (Volume 1: Temperature).
Menendez M, García-Díez M, Fita L, Fernández J, Méndez FJ, Gutiérrez JM. 2014. High-resolution sea wind hindcasts over the Mediterranean area. Clim Dyn. 42:1857–1872.
Myrberg K, Andrejev O. 2003. Main upwelling regions in the Baltic Sea – a statistical analysis based on three-dimensional modelling. Boreal Environ Res. 8(2):97–112.
O'Dea E, Arnold AK, Edwards KP, Furner R, Hyder P, Martin MJ, Siddorn J, Storkey D, While J, Holt J, Lui H. 2012. An operational ocean forecast system incorporating NEMO and SST data assimilation for the tidally driven European north-west shelf. J Oper Oceanogr. 5:3–17.
O'Dea E, Furner R, Wakelin S, Siddorn J, While J, Sykes P, King R, Holt J, Hewitt H. 2017. The CO5 configuration of the 7 km Atlantic margin model: large-scale biases and sensitivity to forcing, physics options and vertical resolution. Geosci Model Dev. 10:2947–2969.
Pontes MT. 1998. Assessing the European wave energy Resource. J Offshore Mech Arctic Eng. 120(4). doi:10.1115/1.2829544.
Pugh DT. 2004. Changing sea levels. Effects of tides, weather and climate. Cambridge University Press. ISBN 978-0-521-53218-1.
Rudels B. 2015. Arctic Ocean circulation, processes and water masses: A description of observations and ideas with focus on the period prior to the international polar year 2007–2009. Progr Oceanogr. 132:22–67.
Seidov D, Antonov JI, Arzayus KM, Baranova OK, Biddle M, Boyer TP, Johnson DR, Mishonov AV, Paver C, Zweng MM. 2015. Oceanography north of 60° N from World Ocean Database. Progr Oceanogr. 132:153–173.
Shum CK, Woodworth PL, Andersen OB, Egbert GD, Francis O, King C, Klosko SM, Le Provost C, Li X, Molines J-M, et al. 1997. Accuracy assessment of recent ocean tide models. J Geophys Res. 102(C11):25173–25194. doi:10.1029/97JC00445.
Simoncelli S, Fratianni C, Pinardi N, Grandi A, Drudi M, Oddo P, Dobricic S. 2014. Mediterranean Sea physical reanalysis (MEDREA 1987-2015) (Version 1) [dataset]. Copernicus Monitoring Environment Marine Service (CMEMS). doi:10.25423/medsea_reanalysis_phys_006_004.
Skagseth Ø. 2008. Recirculation of Atlantic water in the western Barents Sea. Geophys Res Lett. 35. doi:10.1029/2008GL033785.
Suursaar Ü, Aps R. 2007. Spatio-temporal variations in hydrophysical and chemical parameters during a major upwelling event off the southern coast of the Gulf of Finland in summer 2006. Oceanologia. 49(2):209–228.
Tuomi L, Kahma KK, Pettersson H. 2011. Wave hindcast statistics in the seasonally ice-covered Baltic Sea. Boreal Environ Res. 16:451–472.
Turner JF, Iliffe JC, Ziebart MK, Jones C. 2013. Global ocean tide models: assessment and use within a surface model of lowest astronomical tide. Marine Geodesy. 36(2):123–137. doi:10.1080/01490419.2013.771717.
Väli G, Zhurbas V, Laanemets J, Elken J. 2011. Simulation of nutrient transport from different depths during an upwelling event in the Gulf of Finland. Oceanologia. 53(1–TI):431–448. doi:10.5697/oc.53-1-TI.431.
Wekerle C, Wang Q, Danilov S, Schourup-Kristensen V, von Appen W-J, Jung T. (2017). Atlantic WATER in the Nordic Seas: locally eddy-permitting ocean simulation in a global setup. J Geophys Res Oceans. 122:914–940. doi:10.1002/ 2016JC012121.